Characterizing the complexity of microseismic signals at slow-moving clay-rich debris slides: The Super-Sauze (Southeastern France) and Pechgraben (Upper Austria) case studies

Naomi Vouillamoz[1], Sabrina Rothmund[1], Manfred Joswig[1]

[1]Insitute for Geophysics, University of Stuttgart, 70174 Stuttgart, Germany

Correspondence to: Naomi Vouillamoz (naomi.vouillamoz@geophys.uni-stuttgart.de)

Abstract. Soil and debris slides are prone to rapid and dramatic reactivation. Deformation within the instability is accommodated by sliding, whereby weak seismic energies are released through material deformation. Thus, passive microseismic monitoring provides information that relate to the slope dynamics. In this study, passive microseismic data acquired at Super-Sauze (Southeastern France) and Pechgraben (Upper Austria) slow-moving clay-rich debris slides ("clayey landslides") are investigated. Observations are benchmarked to previous similar case studies to provide a comprehensive and homogenized typology of microseismic signals at clayey landslides. A well knowledge of the various microseismic signals generated by the slope deformation is crucial for the future development of automatic detection systems to be implemented in early-warning systems. Detected signals range from short duration (< 2 s) quake-like signals to a wide variety of longer duration tremor-like radiations (> 2 s – several min). Complex seismic velocity structures, low quantity and low quality of available signal onsets and non-optimal seismic network geometry severely impedes the source location procedure, thus rendering source processes characterization challenging. Therefore, we constrain sources location using the prominent waveform amplitude attenuation pattern characteristic of near-source area (< about 50 m) landslide-induced microseismic events. A local magnitude scale for clayey landslides ($M_{L\text{-}LS}$) is empirically calibrated using calibration shots and hammer blows data. The derived $M_{L\text{-}LS}$ returns daily landslide-induced microseismicity rates that correlate positively with higher average daily displacement rates. But high temporal and spatial resolution analyses of the landslide dynamics and hydrology are required to better decipher the potential relations linking landslide-induced microseismic signals to landslide deformation.

1 Introduction

Slow-moving soil and debris slides ~~(Hungr et al., 2014)~~ developed in tectonised marl formations are characterized by seasonal dynamics as well as by sudden (generally rainfall triggered) reactivation and liquefaction phases (Malet et al., 2005; Hungr et al., 2014). The slow deformation of soil and debris slides is expected to generate elastic accumulation and rupture whereby seismic energy will be released within the landslide body. Therefore, passive seismic monitoring is a good approach to monitor and mitigate slope instabilities since it provides high temporal resolution data (sample rates up to 1,000

Hz) in near real-time that relate to the dynamics of the landslide. The transition from steady-state sliding to a rapid transformation of the landslide into a debris flow may be detected and slope failure anticipated.

Seismic investigations of natural and artificial slope instabilities started in the 1960's with acoustic emission (~~AE:~~ 10-1,000 kHz) (e.g. Beard, 1961; Cadman and Goodman, 1967; Jurich and Miller Russell J., 1987) and have been complemented during the last decades by an increasing number of passive microseismic monitoring studies (1-1,000 Hz), carried out in various geological context. The shear boundaries of the Slumgullion earthflow in Colorado were first investigated by Gomberg et al. (1995) as a strike-slip fault zone analog. The study confirmed the existence of detectable brittle deformation processes associated to the slide deformation. In Europe, investigated clayey landslides include the Heumoes slope in the Austrian Vorarlberg Alps (Walter and Joswig, 2008; Walter et al., 2011), the Super-Sauze landslide in the French Southwestern Alps (Walter and Joswig, 2009; Walter et al., 2012; Tonnellier et al., 2013; Provost et al., 2017) and the Valoria landslide in the Northern Apennines in Italy (Tonnellier et al., 2013). Case studies carried out at rockslides include for example the Randa rockslide in the Swiss Alps (Eberhardt et al., 2004; Spillmann et al., 2007); the Åknes rockslide in Norway (Roth et al., 2005; Fischer et al., 2014); the Séchilienne rockslide in the Southeastern French Alps (Helmstetter and Garambois, 2010; Lacroix and Helmstetter, 2011); and the Gradenbach, Hochmais-Atemskopf and Niedergallmigg-Matekopf deep-seated rock slope deformations in the Eastern Austrian Alps (Brückl and Mertl, 2006; Mertl and Brückl, 2007; Brückl et al., 2013).

Observed near microseismic signals (receiver-source distances < 500 – 1,000 m) comprise micro-quake events, for which Gomberg et al. (1995) introduced the term 'slidequake'. Such events have been reported both at rock and debris slides and are inferred to be associated to fracture processes in the host rock, at the sliding surface, or within the landslide body. Rockfalls and rock-avalanches signals were also characterized at steep debris slides and at rock slides (Helmstetter and Garambois, 2010; Walter et al., 2012; Tonnellier et al., 2013; Provost et al., 2017). In addition, a wide variety of tremor signals have been reported marginally (Gomberg et al., 1995; Brückl and Mertl, 2006; Mertl and Brückl, 2007; Spillmann et al., 2007; Gomberg et al., 2011; Walter et al., 2012; Tonnellier et al., 2013; Provost et al., 2017). No common typology has yet been suggested for these signals and the signal source interpretation remains speculative.

This study aims at proposing a classification of microseismic signal types ~~observed~~ as recorded by tripartite microseismic arrays deployed at slow-moving clay-rich debris slides ("clayey landslides"). Tripartite microseismic arrays are suited for the determination of the back azimuth and apparent velocity of an incoming signal, hence providing key information about the signal source location (e.g. Joswig, 2008; Sick et al., 2012; Vouillamoz et al., 2016). The classification of microseismic signals is based on ~~simple~~ waveform and spectral attributes of the signals and ~~using~~ uses microseismic observations reported by similar case studies as a benchmark. Because of the lack of clear phase arrivals and signal coherence across the seismic network at clayey landslides, standard seismological approaches to source location using arrival times derive minimum uncertainties of ± 50 m for near-source area microseismic events (e.g. Tonnellier et al., 2013). Therefore, we apply an alternative method based on seismogram amplitude information to constrain the receiver-source distance of near-source area landslide-induced microseismic events. The technique is generally referred in the literature as amplitude source location,

ASL, and has been used following various approaches to locate microseismic sources recorded at distances of less than a few kilometers at volcanoes (e.g. Jolly et al., 2002; Battaglia, 2003; Battaglia et al., 2005) or glaciers (e.g. Jones et al., 2013; Röösli et al., 2014), as well as for different kinds of mass motion, including lahars (e.g. Kumagai et al., 2009) and debris flows (e.g. Walter et al., 2017). We applied a simple ASL approach in which calibration shots and hammer blows carried out in the study area were used to evaluate amplitude attenuation patterns empirically. Then, with the aim to reduce bias and errors in the estimation of landslide-induced microseismicity rates, the distance attenuation function of the local magnitude scale was calibrated for clayey landslides using the active microseismic datasets. Detected microseismic events were finally gathered in a comprehensive catalog. The final catalog of landslide-induced microseismic signals provides an important basis for a multidisciplinary comparative analysis with other landslides observations such as displacement, cracks and fissures development, or hydrometeorological data to gain knowledge about landslide dynamics, as well as an initial signals library to train automatic detection and classifier systems.

2 Data

Seismic measurements were acquired at two well-instrumented slopes: The Super-Sauze (Southwestern French Alps) and Pechgraben (Upper Austria) landslides (Fig. 1a-b). Both instabilities are characterized by a clay-rich matrix transporting rigid boulders of marls and limestones (including leftovers and remains of vegetation at Pechgraben) with moving rates ranging between a few mm up to several tenths of cm per day in the investigated areas and periods (Fig. 1c-d). In the monitored areas, the thickness of the instability reaches more than 10 m at Super-Sauze, but do not exceed a few meters (2-4 m) at Pechgraben. More details about the two landslides can be found in Malet (2003); Travelletti (2011); Tonnellier et al. (2013) for Super-Sauze and Lindner et al. (2014); Lindner et al. (2016) for Pechgraben.

Continuous data of three seismic campaigns were investigated (Fig. 1):

- **Super-Sauze 2010 (SZ10)**: May 28–July 24, 2010; 58 days; 18 sensors in 2 ha; average displacement of 0.4 cm d^{-1}, obtained by daily dGNSS (differential global navigation satellite system) measurements.
- **Pechgraben 2015 (PG15)**: October 7-15, 2015; 9 days; 12 sensors in 6 ha; average displacement of 2 cm d^{-1}, obtained by weekly dGNSS measurements.
- **Pechgraben 2016 (PG16)**: November 8-12, 2016; 5 days; 12 sensors in 1 ha; average displacement of more than 20 cm d^{-1}, estimated by triangulation, using grids of fixed nails both on the stable and on the active part of the slide and daily photo-monitoring.

Tripartite seismic arrays were deployed with station spacing of 5-50 m (Fig. 1c-d). Each seismic array consists of a central three-component (3-C) short-period seismometer (Lennartz 3Dlite) which is surrounded by three to six vertical short-period seismometers (Lennartz 1Dlite). The seismometers were buried about 30 cm deep in the landslide material. Data were collected by battery powered SUMMIT M Hydra data loggers. At Super-Sauze, the array S3 consists of Noemax Agécodagis velocimeters (one 3-C and six verticals) with associated band-pass of 0.1-80 Hz, connected to a Képhren Agécodagis

acquisition system powered by solar panels. This array is part of a permanent monitoring installation (National French Landslide Observatory Facility and RESIF Datacenter, 2006). The seismometers feature therefore a robust installation and are housed in plastic drums on top of a concrete slab. A comparison of the data collected by the different installation systems proved consistent: identical waveforms featuring similar amplitudes are observed for microseismic events recorded at the co-located stations S1.5, S2.6 and S3.6; local, distant and tele ~~-earthquakes~~seisms are recorded with similar amplitudes across the complete seismic network. No significant difference in terms of waveform scattering was found for signals recorded by stations installed in the more stable areas. At Pechgraben, ~~D~~due to the relatively large aperture (30-50 m) of the ~~PG15~~ seismic arrays in the PG15 campaign, many near-source area microseismic events were recorded by less than three sensors. Consequently, a denser seismic network configuration was designed for the PG16 campaign. Inherent difficulties of operating systems continuously on landslides resulted in partially incomplete datasets (Fig. 1e). This aspect must be considered when evaluating the completeness of landslide-induced microseismic catalogs.

3 Method

Data were analyzed following the "*Nanoseismic Monitoring*" methodology using the NanoseismicSuite software package developed at the Institute for Geophysics of the University of Stuttgart (Wust-Bloch and Joswig, 2006; Joswig, 2008; Sick et al., 2012; Vouillamoz et al., 2016). The method is supported by a realtime, analyst-guided interactive multi-parameter visualization approach. First, signals are identified by visual screening of continuous sonogram, where sonograms are logarithmically scaled spectrograms featuring a dynamic frequency-dependent noise adaptation (Joswig, 1990, 1995, 1996). The enhanced visualization of sonograms has unmatched power to facilitate the detection and recognition of various types of weak signal energies in low-SNR (signal-to-noise ratio) conditions without a-priori knowledge (Joswig, 1990; Sick et al., 2012; Vouillamoz, 2015; Vouillamoz et al., 2016; Sick, 2016). The SonoView module of the NanoseismicSuite software provides a dynamic layout, where single-trace sonograms or multi-trace (array-stacked) super-sonograms are visualized on a common timeline, with up to several hours in one laptop screen. Different resampling can be applied to the data, facilitating the focus on various event types (short/long duration, low/high frequency). Detected events are tagged and synchronized in the linked HypoLine module of the software suite for further evaluation. There, waveforms are analyzed interactively to provide an optimized graphical hypocentral solution. Seismograms can be simultaneously processed in network and array mode, taking advantage of the tripartite configuration of the seismic mini-arrays (see Joswig (2008) and Vouillamoz et al. (2016) for a comprehensive description of the HypoLine software). The strength of the method is its ability to easily detect and successfully evaluate any kind of signals without a-priori knowledge in noisy environment. The drawback is that the process is not automated. It is therefore time-consuming and not well-suited for large datasets (years). Results may also not be reproducible to 100 %.

Much attention was paid to design a comprehensive database gathering all microseismic signals observed by passive microseismic monitoring on active debris slides. Continuous sonograms of the three seismic datasets (SZ10, PG15, PG16)

were visually screened in SonoView. To avoid false noise detection, special attention was paid when screening day-time measurements contaminated by anthropogenic noise caused by geophysicists or geotechnical work carried out on the slope. Only signals recorded coherently by three sensors at least were declared as a detection. Each detection was first evaluated individually and interactively in HypoLine, where phases information were picked, and time offsets between array-correlated wave~~- front~~ packets used to derive apparent ~~velocities~~ velocity and back azimuth~~ calculated~~ information following the approach described in Figure 5 of Vouillamoz et al. (2016). Then, waveform and spectral features of all signals were analyzed semi-quantitatively using MATAB® routines: (1) For each event, all vertical trace seismograms of the seismic network were visualized on a common timeline with normalized and non-normalized amplitudes, using a set of pre-defined time windows (5, 10, 30, 60 and 120 s). The signals coherency, the event duration and the waveform amplitude attenuation pattern across the seismic network were checked. (2) Traces on which the signal of interest is contaminated by noise and traces that did not record the event were tagged and discarded from further analysis. (3) For each trace that recorded the event, the non-logarithmic spectrogram, the unfiltered waveform and a series of waveforms with selected band-pass filter were plotted and evaluated. (4) The amplitude spectrum (FFT, fast Fourier transform) was calculated to estimate the dominant frequency content of the signals. ~~In our case,~~Since the short receiver-source distances of the considered signals do not allow a clear separation of body waves and surface waves~~. Therefore,~~ amplitude information was taken as the maximum absolute 0-to-peak amplitude of the signal unfiltered vertical seismogram.

3.1 Classification

Potential landslide-induced microseismic events were finally classified considering the following ~~simple waveform and spectral~~ features:

- **Apparent velocity of trackable wave packets**. Well-constrained apparent velocities (computed by array processing for wave packets showing at least four traces with correlation thresholds > 70 %) range from less than 0.2 km s^{-1} to more than 5.0 km s^{-1}. We distinguish two main classes of apparent velocities: < 2.0 km s^{-1} (top most volume of the landslide body and landslide body) and > 2.0 km s^{-1} (sedimentary bedrock), in agreement with published velocity profiles at clayey landslides (Williams and Pratt, 1996; Tonnellier et al., 2013).
- ~~**Unique versus multiple**~~**Clustering of events**. Single events are distinguished from events featuring multiple jolts and repeated energic spikes.
- **Signal duration in seconds**. Signals are classified in three duration classes: short duration (< 2 s); medium duration (2-20 s); and long duration signals (> 20 s - minutes).
- **Amplitude attenuation pattern**. The signals of landslide-induced microseismic sources are expected to be severely attenuated, mainly because of their ~~source proximity and their~~ propagation through heterogenous clay-rich soils of various water saturation (e.g. Koerner et al., 1981). Calibration shots and hammer blows carried out at Super-Sauze and Pechgraben showed that sources occurring within the seismic network feature prominent waveform attenuation across the seismic network, whereas sources originated a few hundred meters outside the seismic network feature

waveforms being homogeneously attenuated, resulting in similar signal amplitudes across the seismic network. ~~Assuming that the decrease in the seismic amplitude is proportional to the inverse of the distance from the source for body waves or to the inverse of its square root for surface waves (e.g. Yamasato, 1997; Battaglia, 2003),~~ Therefore, only ~~those~~ microseismic events featuring prominent and consistent attenuation of the signal maximum amplitudes across the seismic network are considered as a nearby source, potentially induced by the landslide dynamics. ~~In our case, the short receiver-source distances of the considered signals do not allow a clear separation of body waves and surface waves. Therefore, amplitude information was taken as the maximum absolute 0-to-peak amplitude of the signal unfiltered vertical seismogram.~~

- **Frequency-related characteristics**. The distribution of the dominant energies at individual station records is evaluated in the signal spectrogram, in a selection of band-passed filtered waveforms (1-5; 5-20; 20-50; 50-100 and 100-200 Hz) as well as in the amplitude spectrum. Signals with dominant energies mainly below 50 Hz are separated from events featuring dominant energies well above 50 Hz. Additional observed characteristics include harmonic peaks, dispersive, gliding or multiple-band dominant frequencies. These frequency-related characteristics are illustrated in the event classification (Section 4).

Based on these features and using previous studies (Gomberg et al., 1995; Walter and Joswig, 2008, 2009; Gomberg et al., 2011; Walter et al., 2012; Tonnellier et al., 2013; Provost et al., 2017) as a benchmark, microseismic events detected at clayey landslides are gathered in three main groups that we describe and discuss in the Section 4:

1. Earthquakes (local, regional and teleseism~~sic~~).
2. Quakes (receiver-source distance < 50-500 m).
3. Tremors (landslide-induced tremor signals and external sources of tremor-like radiations).

4 Unified microseismic signals typology at clayey landslides

To help the reader in the comparison of the different microseismic signals, we apply the layout of Figure 2, which illustrates an earthquake signal, for all representative events of the classification (only vertical traces are used):

a. Shows the signal sonogram (Joswig, 1990) up to the Nyquist frequency with a logarithmic ordinate, which corresponds to ~~of~~ 1.95-250 Hz for Pechgraben data and to 3.91-500 Hz for Super-Sauze data. Darker colors indicate higher relative energies.

b. Displays the non-logarithmic spectrogram of the signal with an ordinate up to 250 Hz. The time-window is taken as the signal length divided by 30 and an overlap of 90 % was applied. Red colors indicate higher energies in dB. Both the MATLAB® spectrogram code and colormap were provided by Clément Hibert, of the EOST (Ecole et Observatoire des Sciences de la Terre), University of Strasbourg, France.

c. Provides the unfiltered seismogram with maximum absolute 0-to-peak amplitude indicated above the trace in nm s^{-1}.

d. Shows from bottom to top band-pass filtered waveforms of the signal between 1-5, 5-20, 20-50, 50-100 and 100-200 Hz, defined as bp1 to bp5. A second order Butterworth filter is applied. Maximum absolute 0-to-peak amplitudes are indicated in nm s^{-1} above each respective trace.

e. Displays the amplitude spectrum in nm Hz^{-1}, computed by FFT for the time window indicated by the red bar in (d). A reference horizontal line at 100 nm Hz^{-1} help event comparison.

4.1 Earthquakes (local, regional and teleseismic)

Local, regional and teleseismic earthquakes are detected daily by seismic networks. Because earthquakes are potential trigger of landslides, it is important to catalogue these events. Seismic features of earthquakes are well known from routine seismogram analysis. At clayey landslides, earthquakes produce medium to long duration signals that are recorded with similar amplitudes across the complete seismic network. The duration and strength of an earthquake signal as well as its frequency content vary as a function of source distance and magnitude. Sharp and broadband distribution of initial frequency content is typically followed by a decrease in frequency content of the signal energy with successive phase onsets, resulting in a typical triangular-shaped sonogram pattern for earthquakes. Onsets of high-SNR events are impulsive. Individual phases with moderate scattering can be identified and return apparent velocities above 2.0 km s^{-1} (Table 1, Fig. 2).

4.2 Quakes

4.2.1 Previous observations

Quake signals have been observed in previous studies carried out at clayey landslides. Gomberg et al. (1995) and Gomberg et al. (2011) report short-duration earthquake-like signals, with clearly discernable, trackable wave packets that they refer as slidequakes. Dominant frequencies of slidequakes are not stated, but can be evaluated visually between 10 and 100 Hz based on the waveforms displayed in Figures 5 and 6 of Gomberg et al. (2011). Walter et al. (2012) describe earthquake-like events with duration of up to 5 seconds and associated frequency content of 10-80 Hz, which they refer as slidequakes after Gomberg et al. (1995). Tonnellier et al. (2013) and Provost et al. (2017) report quake-like signals with duration of about one second, dominant frequencies around 10 Hz, emergent first arrivals and undistinguishable P- and S-waves.

4.2.2 Updated classification of quake signals

Based on waveform amplitude attenuation pattern, duration and dominant frequency content of the signals, we propose four types of quake events (Table 1; Fig. 3 and Fig. 4).

- **Type I – Near high-frequency quakes.** Signals show durations of less than 1 s and are recorded only at a few nearby stations, suggesting a nearby source (Fig. 3a). Waveform amplitudes show strong attenuation (Fig. 3e). Maximum absolute amplitudes of about 10,000 nm s^{-1} were observed. High-SNR signals feature impulsive onsets. Dominant frequencies of the highest amplitude traces are in the 20-100 Hz range (spectrogram, band-pass filtered

waveforms and amplitude spectrum in Fig. 4a and 4e (upper panel)). P- and S-phases cannot be clearly distinguished; however, successive phases may be identified based on the apparent velocity of trackable wave packets that scale within 0.2-1.8 km s^{-1}.

- **Type II – Near low-frequency quakes**. Signals have duration of 1-2 s and are recorded by the complete seismic network with strong amplitude attenuation, suggesting a nearby source (Fig. 3b and 3e). Maximum amplitudes of a few 10,000 nm s^{-1} were observed. Dominant frequencies of the highest amplitude signals stay typically in the 5-50 Hz range (spectrogram, band-pass filtered waveforms and amplitude spectrum in Fig. 4b and 4e~~,~~ (lower panel)). The signals ~~consist of~~appear as prominent and scattered surface waves that can be tracked over the seismic network. P- and S-phases cannot be clearly distinguished, but successive phases can eventually be discriminated based on the apparent velocity of trackable wave packets that range within 0.2-1.8 km s^{-1}.
- **Type III – Moderate distance quakes**. Signals last 2.0-2.5 s and are recorded by the complete seismic network with consistent amplitudes across the seismic network suggesting a source outside of the seismic network (Fig. 3c and 3e). Most events feature low amplitudes and are recorded just above the noise threshold (100-500 nm s^{-1}). Dominant frequencies are in the 5-50 Hz range, but weak signal energies are typically found within 50-100 Hz at the onset of the events (spectrogram, band-pass filtered waveforms and amplitude spectrum in Fig. 4c). Apparent velocities of scattered wave packets range within 1.5-2.0 km s^{-1}. P- and S-phases are difficult to identify.
- **Type IV - Local micro-quakes**. Signals have duration of 2-10 s and are recorded by the complete seismic network with similar amplitudes (Fig. 3d-e). Successive phases can be tracked consistently over the seismic network with apparent velocity ranging within 2.0-5.0 km s^{-1}. Dominant frequencies are in the 5-50 Hz but signal onsets generally display energies in the 50-100 Hz (spectrogram, band-pass filtered waveforms and amplitude spectrum in Fig. 4d). P- and S-phases can be identified.

4.3 Tremor signals

4.3.1 Previous observations

Various tremor-like signals were observed at clay-rich instabilities. Gomberg et al. (1995) and Gomberg et al. (2011) report episodes of tremor-like radiation and sinusoidal waveforms lasting tens of minutes and coherent across the seismic network, which they infer as ETS (episodic tremor and slip) analog of strike-slip faults. A deeper analysis showed that many of these signals feature gliding spectral lines above 50-100 Hz in the spectrogram. Although gliding frequency tremors are known under 20 Hz at volcanoes and inferred to image change in the source properties (e.g. Hotovec et al., 2013; Unglert and Jellinek, 2015; Eibl et al., 2015 and references therein), gliding harmonics are also characteristic of environmental noise signals produced by moving vehicles such as airplanes or helicopters (e.g. Biescas et al., 2003; van Herwijnen and Schweizer, 2011; Eibl et al., 2015; Eibl et al., 2017). There, the gliding harmonics correspond to the Doppler shift produced by a moving source passing a stationary receiver. At Slumgullion landslide, Gomberg et al. (2011) interpret gliding

frequency tremors in the 50-100 Hz range as generated by the action of moving vehicles along a distant (several km) road. However, a slide-generated source (slow rupture of faults or materials entrained within the faults like trees or boulders, or slow basal slip) is not excluded for tremor-like radiation devoid of gliding frequency and featuring the highest amplitudes at the seismic network most remote location from the road. These events last several minutes and show dominant energies distributed broadly above 30-50 Hz and diminishing toward the Nyquist at 125 Hz (Gomberg et al., 2011).

At Super-Sauze and Valoria landslides, tremor-like signals lacking clear onsets and with undistinguishable phases were observed with duration of a few seconds to tens of seconds (Walter et al., 2012; Tonnellier et al., 2013; Provost et al., 2017). Spiky, cascading signals are interpreted as rockfalls. Such events feature repeated jolts in the 10-30 Hz that correspond to the rockfall impacts, as well as a 'noise band' in the 30-130 Hz range, likely generated by fine-grain material flows. These events are normally well recorded across the complete seismic network, with moderate waveform amplitude attenuation and maximum amplitudes reaching 1,000-10,000 nm s^{-1}. High-frequency tremor-like signals with duration of less than 20 s and maximum amplitudes under 10,000 nm s^{-1}, featuring drastic waveform amplitude attenuation and thus recorded only partially across the seismic network were also observed (Walter et al., 2012; Tonnellier et al., 2013). Walter et al. (2012) showed that the occurrence rate of these signals correlates well with the measurements of an extensometer installed about a fissure and co-located with a 1-C seismometer at Super-Sauze, July 2009. They concluded that such signals must be triggered by fissure formations at the surface of the landslide, but also considered scratching and grinding of landslide material against (emerging) hard rock crests as a potential source.

4.3.2 Updated classification of tremor signals

As in previous studies, a wide range of tremor-like signals were recorded at SZ10, PG15 and PG16. Short and medium duration (< 20 s) events are distinguished from long duration, minute-long lasting sequences of tremor-like radiations (Table 1). While short and medium duration events feature trackable wave packets consisting of spikes or jolts, minute-long lasting sequences are characterized by sinusoidal waveforms and gentle rumbles, that are difficult to track coherently across the seismic network. Due to the general waveform intricacy and the wide range of observed dominant frequency, finding an unequivocal classification for tremor events is difficult. Based on the literature and searching for consistent observations at SZ10, PG15 and PG16 we propose the following typology of tremor events, where landslide-induced tremor-like signals are distinguished from external sources of tremor-like radiations. Among the landslide-induced events, signals potentially generated by deformation and stick-slip within the landslide body are separated, when possible, from tremor-like signals originating from exogenous landslide dynamics such as rockfalls or small debris flows. Since anthropogenic noises share similarities in waveform amplitudes and in spectral content with landslide-induced tremor signals, it is important to gain knowledge about the characteristics of such events for the manual and automatic detection of landslide-induced tremor signals.

- **ETS-like signals.** Microseismic signals showing similarities to ETS signals at strike-slip faults were observed. ETS-like signals at debris slides are emergent and cigar-shaped, last a few seconds and are strongly attenuated

across the seismic network (Fig. 5b and 5d~~,~~ (top panel)). They occur typically in temporal sequences. Dominant frequency of the highest amplitude signals range within 5-50 Hz (spectrogram, band-pass filtered waveforms and amplitude spectrum in Fig. 6a and 6d~~,~~ (top panel)). Maximum observed absolute amplitudes reach some 10,000 nm s^{-1}; however, most events show amplitudes no higher than a few 100-1,000 nm s^{-1}. Phases cannot be identified, instead, the waveforms feature repeating and intricated spikes or jolts with prominent scattering. Individual wave packets which can be tracked return apparent velocity below 2.0 km s^{-1}.

- **Confirmed rockfall events.** Signals generated by rockfalls resemble ETS-like signals (compare Fig. 5b and 5d with Fig. 6b and 6d~~,~~ (top panel)). The impacts of falling blocks produce spikes or jolts in the waveforms; loose material saltation and flow combined to the moving character of the source increase waveform intricacy. Signal duration and dominant frequency, as well as waveform amplitude attenuation pattern vary significantly depending on the size of the rockfall event and its distance to the recording seismic network. Apparent velocities derived for individual impact signals remain below 2.0 km s^{-1}. Because rockfalls are exogenic, potential source areas are known from field observations. In addition, the signal source can eventually be caught by field observations or remote sensing. At SZ10, one landslide-induced tremor signal could be matched with a single-marl block failure event caught in a high-repetition rate UAV imagery (unmanned aerial vehicle) and optical ground-based images (Rothmund et al., 2017).
- **Harmonic tremors.** Signals lasting a few seconds and consisting of narrow frequency band harmonic peaks were observed at SZ10, PG15 and PG16 (Fig. 5a, 5c and 6c). The main harmonic is generally found around 8-10 Hz, followed by several multiples of lower energies (Fig. 6c, amplitude spectrum). Maximum absolute 0-to-peak amplitudes do not exceed a few 100-1,000 nm s^{-1}, and most signals lie barely above the noise threshold. At SZ10, harmonic tremors were observed only at single sensors. At Pechgraben, harmonic tremors were detected with various waveform amplitude attenuation pattern across the seismic network, suggesting a non-unique source location origin for these signals. Because of the harmonics, apparent velocities are difficult to calculate. For high-SNR signals, apparent velocities calculated with the first arrivals derived velocities of less than 0.7 km s^{-1}. Harmonic tremors occur typically in minute-long lasting sequences, alternating with ETS-like signals (Fig. 4a-c).
- **Dispersive tremors.** Several instances of long duration (few minutes) dispersive tremor-like signals were detected at SZ10, PG15 and PG16. Due to the dispersive character of the signals, the waveforms and spectrograms feature important variations from one station to another, rendering the events difficult to detect. The Figure 7a shows an example of a dispersive tremor well recorded across the seismic network at SZ10. The high amplitudes (> 20,000 nm s^{-1}) and dominant frequency content above 50 Hz at station S3.7 (spectrogram, band-pass filtered waveforms and amplitude spectrum in Fig. 7a~~,~~ (top panel)) suggest a source origin close to that station. Then, with increasing distance to the most probable source area (receiver-source distances indications above the sonograms in Fig. 7a), the signals show prominent dispersion and waveform amplitude attenuation. Apparent velocities calculated at the signal onset range within 0.3-0.5 km s^{-1}, close to the velocity of sound in the air or velocities in the top most layer

of the landslide (e.g. Tonnellier et al., 2013). The temporal evolution of the dominant frequency content of the signals and the waveform envelopes, well observed in the spectrograms of Figure 7 and in the waveforms of Figure 8a, show similarities to signals produced by mass movement (e.g. Yamasato, 1997; Biescas et al., 2003) or by persons walking about the seismic network (waveforms in Fig. 8a-b and spectrogram in Fig. 9a) and hence suggest a moving source.

- **External sources of microseismic noise and tremor-like radiations.** Shallow installations of the seismometers in clayey materials result in important noise contamination of the seismograms, especially in the high frequency range (> 50 Hz). The variety of events produced by external source of noise is large. Signals range from short to long duration. In common to all signals is the absence of identifiable successive phases. Individual wave packets are difficult if not impossible to track. Thus, apparent velocities cannot be calculated. Maximum waveform amplitudes can reach several 10,000-100,000 nm s^{-1} and waveform amplitude attenuation patterns are incoherent. The most common microseismic signals produced by external source of noise are presented in Figures 8 and 9. Nearby (< 50-100 m) moving source such as geophysicists walking about the stations produce long duration spiky tremor radiations (Fig. 8b). Typical of such local moving source is the change towards higher frequency of the dominant energies of the signal as the source (the person walking) is approaching the recording station and the change towards lower frequency content of the dominant energies of the signal as the source is getting further away (sonogram and spectrogram in Fig. 9a). Distant moving sources such as airplanes and vehicles passing on nearby roads, produce long duration cigar-shaped seismograms and spectrograms with typical gliding harmonics in the 50-200 Hz range (Fig. 7b, 8c and 9b). Beside anthropological noises, many environmental sources of noise were recorded but could not necessarily be distinguished in the absence of additional data at SZ10, PG15, and PG16. Wind bursts, rainfall and storms as well as water streams and bedload transports all produce long duration tremor-like radiations. Maximum amplitudes can reach several 10,000 nm s^{-1} and waveform amplitude attenuation pattern across the seismic network is incoherent (Fig. 8d). These events illuminate either several frequencies or only specific ones in the spectrograms (see also Provost et al., 2017) and the spectrograms are clearly devoid of gliding harmonics (Fig. 9c-d).

5 Microseismic source characterization

5.1 Source location

Seismic velocities and source location quality can be estimated and verified using calibration shots or hammer blows. Calibration shots and hammer blows were carried out at SZ10 and PG16 and could be located with average accuracies of about ± 50 m, when using all available first arrivals and back azimuth information with a half-space velocity model. Our results concur with previous results by Tonnellier et al. (2013) at Super-Sauze landslide, where uncertainties of 40-60 m where estimated for calibration shots carried out within the seismic network. It is worth mentioning that this corresponds to

the size of the seismic network and scales with the landslide dimension. Thus, even if the seismic network is dense, locating landslide-induced microseismic sources in clayey landslides and discriminating between a source originated within or outside the landslide body is challenging: (1) The velocity structures show drastic variations in short distances (complex material mélange, topography), and also evolves with time (slope deformation, hydrological state). Velocity models are thus only approximated by tomographic analysis for a specific time (Fig. 10a-b). (2) Scattering and attenuation of the waveforms result in low-SNR onsets where phases are difficult (if not impossible) to identify. (3) The seismic network geometry relative to the source is in most natural cases not optimal. (4) With an average station spacing of 5-50 m, as it is the case in our study, most landslide-induced microseismic events show no more than four unambiguous phase information.

We used HypoLine (see Section 3) to simulate and analyze graphically the contribution of these parameters on the epicentral location solutions of calibration shots (SISSY, Seismic Source Impulse System, developed by the LIAG, Leibniz-Institut für Angewandte Geophysik, Germany~~http://www.liag-hannover.de/s/s1/a1/sissy, last accessed September 13, 2017~~) at SZ10 (Fig. 10). Three layered v_P velocity models simplified from Tonnellier et al. (2013) and featuring both higher and lower velocity contrasts between the landslide material and the sedimentary host rock were tested (Fig. 10a-b; Table 2). For each pair of first arrivals, the time-reversal hyperboles (hypolines) were computed at depth zero. To image the weight of phase uncertainties on the epicenter solutions, all hypolines were also computed for two shifted values of the first arrival by ± five samples (Fig. 10c). An epicenter solution is found at the highest concentration of hyperboles intersections (see Joswig, 2008 and Vouillamoz et al., 2016 for details). The exercise was carried out for the three velocity models and the resulting epicenter solutions were analyzed for different station combinations. The Figure 10d shows the results obtained when using first arrivals of the three seismic arrays individually. The outcomes of this analysis can be summarized as follow:

- The applied velocity model has low impact on the epicentral solution (few meters) within the considered station network or in small distances. However, outside of the seismic network, solutions diverge significantly.
- Five samples (±) uncertainties at 1,000 Hz correspond to a high-quality phase onset pick in routine earthquake catalogs (e.g. Diehl et al., 2009). Such high-quality phase onsets derive consistent solutions within the considered station network, but the solutions also diverge significantly outside of the considered seismic network.
- First arrivals of natural sources are of lower quality than those of calibration shots (Fig. 10c). Lower quality onsets have an important impact on the epicentral solutions. At ± 20 samples (± 0.02 s), no more mathematical existent solution is found!
- The seismic network geometry relative to the source has the most significant influence on the location solution. Whereas the epicenter is resolved with uncertainties of about 20 m when using a set of stations surrounding the calibration shot (Fig. 10d~~,~~ (central panel)), the potential location solutions are biased by 50 m and more when using a station network that do not surround the source (Fig. 10d~~,~~ (left and right panels)).
- First arrivals at stations in tripartite configurations derive three zones of high-density hyperboles intersections that cannot be discriminated without additional constraints such as back azimuth information (beam-processing).

- Complex velocity structures and resulting waveforms scattering impedes array processing and back azimuth information can be significantly biased. The calibration datasets at Super-Sauze and Pechgraben derive uncertainties in the order of one quadrant (± 45°) for well constrained beams (using high correlation values of four and more coherent waveform spikes), for source located at 50-100 m outside of the seismic mini-array.
- Sources originated within the seismic network return incoherent array processing and back azimuth data.

Thus, it can be concluded that approximation in the velocity model, low-quality first arrivals and non-optimal seismic network geometry at clayey landslides result in natural source location uncertainties ranging from tens of meters for sources originated within the seismic network to hundreds of meters for sources originated outside of the seismic network. Consequently, the risk of including biased data in maps of landslide-induced microseismicity is high. Moreover, the estimation of the magnitude has a logarithmic dependence to the receiver-source distance. Thus, high uncertainties (> 50-100 m) held in the source location can affect the magnitude calculation by several orders of magnitude units.

5.2 Amplitude attenuation pattern to constrain receiver-source distance

Because of the high uncertainties returned by arrival-time based approaches to event location, the drastic attenuation of waveforms amplitude observed within the landslide body was used to constrain the source proximity of near-source area landslide-induced microseismic events to be used in the calculation of events local magnitude. Distance attenuation data of SISSY calibration shots and hammer blows at Super-Sauze and Pechgraben show that signals are strongly attenuated within the first 50 m. The water content of the landslide material influences the waveform amplitude attenuation: signals are less attenuated when dryer conditions prevail (Fig. 11a). This observation is consistent with laboratory experiments (e.g. Koerner et al., 1981). To quantify the waveform amplitude attenuation pattern of an event, we use the scatter about the median amplitude, S, which we compute for each trace that recorded the signal as Eq. (1):

$$S = \frac{A_{sta} - Med(A_{sta})}{Med(A_{sta})} \times 100\ \% \quad (1)$$

where A_{sta} is the station maximum absolute vertical trace amplitude of the signal in nm s^{-1} and $Med(A_{sta})$ is the median value of all A_{sta} where the signal was recorded. S values computed for the calibration dataset of Figure 11a show a drastic diminution with increasing receiver-source distances (Fig. 11b). Based on these observation, we use maximum S values of landslide-induced microseismic events to approximate receiver-source distances. We infer S values higher than 200 % to correspond to receiver-source distance of less than about 50 m. At smaller distances, we selected thresholds (in an arbitrary, but conservative way) of 1,000 % and 2,000 % to correspond respectively to receiver-source distances of about 20 m and 10 m from the recording station. The source distance of natural events for which S values remain below 200 % is considered as uncertain. Since S values of teleseisms and distant earthquakes were observed to be very stable (< 100 %), no correction for site effects was applied. Among the inferred landslide-induced microseismic events (quakes and tremors), 48 % of events at SZ10, 24 % at PG15 and 39 % at PG16 feature at least one station with a scatter about the median amplitude value above 200 %. With estimated source-receiver distance of less than about 50 m, these events can be reasonably assumed as

originated within the landslide body or at its edges (see Section 6.3) and are used in the local magnitude catalog of landslide-induced microseismic events.

5.3 Calibrating the local magnitude (M_L) scale at clayey landslides

Richter (1958) defines the earthquake local magnitude scale M_L as Eq. (2):

$$M_L = log_{10}(A_{WA}) - log_{10}(A_0) \quad (2)$$

where A_{WA} is originally the half of the maximum peak-to-peak amplitude in microns recorded on a Wood-Anderson (WA) seismograph and $\log_{10}(A_0)$ is the distance attenuation function; i.e. a correction applied for the attenuation of the waveforms with distance. The scale is defined so that a M_L 3 earthquake writes a record of 1 mm peak amplitude on a WA seismograph at a receiver-source distance of 100 km. The distance attenuation function of the M_L scale has been calibrated empirically for earthquakes in many regions around the world (e.g. Bakun and Joyner, 1984; Hutton and Boore, 1987; Stange, 2006; Edwards et al., 2015); however, standard calibrated receiver-source distances range within 10-1,000 km (Fig. 12a). Therefore, these distance attenuation functions are unappropriated for near-source area microseismic events at landslides. Wust-Bloch and Joswig (2006) calibrated a distance attenuation function within 30-300 m for sinkhole events in the Dead Sea valley. Its slope is very similar to extrapolated distance attenuation function at distances of less than 1 km (Fig. 12b).

We calibrated M_L in clayey landslides ($M_{L\text{-}LS}$) by defining the slope and the intercept of the simplest form of the distance attenuation function (Eq. (3)):

$$log_{10}(A_{0-LS}) = slope \times log_{10}(D) + intercept \quad (3)$$

where $\log_{10}(A_{0\text{-}LS})$ is the distance attenuation function in landslides and D is the receiver-source distance in km. The slope is defined using the MATLAB® *logfit* function (© 2014, Jonathan C. Lansey), which returns regression in the form $Y = 10^{intercept}X^{slope}$ for the calibration datasets presented in Figure 11a. An average slope value of -1.75 is found for the different regression curves and taken for $\log_{10}(A_{0\text{-}LS})$ (Fig. 12b).

The intercept of $\log_{10}(A_{0\text{-}LS})$ is then calculated as follow:

1. The theoretical moment magnitude M_w of a SISSY calibration shot is estimated following the Gutenberg-Richter magnitude energy relation, where $\log_{10}(E) = 1.5M_w + 11.8$, E being the radiated seismic energy in ergs. Using E = 240 kJ (~~SISSY working principle, http://www.liag-hannover.de/en/s/s1/a1/sissy/project-presentation.html, last visited September 21, 2017~~SISSY product information sheet), we find $M_{w\text{-}SISSY} = 0.39$.
2. Following Deichmann (2017), we derive M_L of a SISSY shot as $M_{L\text{-}SISSY} = 1.5M_{w\text{-}SISSY} = 0.58$.
3. The intercept of $\log_{10}(A_{0\text{-}LS})$ is found using $M_{L\text{-}SISSY} = 0.58$ with the mean slope of the regression curves (-1.75) and the average maximum absolute vertical trace 0-to-peak amplitude of the calibration shots in 1 m distance ($A_{LS} = 5e10^6$ nm s^{-1}).

The calibrated local magnitude scale $M_{L\text{-}LS}$ in clayey landslides finally writes as Eq. (4):

$$M_{L-LS} = log_{10}(A_{LS}) + 1.75log_{10}(D) - 0.87 \quad (4)$$

where A_{LS} is the maximum absolute vertical trace 0-to-peak amplitude of the signal in nm s^{-1} and D the receiver-source distance in km.

The calibrated distance attenuation curves are steeper than the average slope of regional earthquakes $-\log_{10}(A_0)$ curves (Fig. 12b). However, since no simple relation exist between A_{WA} in mm as used in the calculation of standard M_L and A_{LS} in nm s^{-1} as read on a detection trace in landslides, the comparison of standard distance attenuation functions $\log_{10}(A_0)$ with $\log_{10}(A_{0\text{-}LS})$ is not straightforward. Well imaged in Figure 12b, is the strong influence of various water saturation of the landslide material prevailing during the different calibration measurements, which can result in bias of one order of magnitude or more at distances smaller than 100 m. The range of potential M_L of landslide-induced microseismic events is evaluated in Figure 13. $M_{L\text{-}LS}$ is plotted as a function of the amplitude read in nm s^{-1} using $\log(A_{0\text{-}LS})$ for three receiver-source distances (1, 10 and 100 m). Considering the range of observed signal amplitudes, the graphic shows that landslide-induced microseismicity must scale within about $-3.0 < M_{L\text{-}LS} < 1.0$. This agrees with the potential magnitude range that can be inferred from field observations and assumptions, where active seismogenetic structures are expected to fall in the decimeter-meter range.

6 Discussion of microseismicity catalogs at clayey landslides

6.1 Passive seismic monitoring at clayey landslides

Progresses in environmental seismology are driving geophysicists and seismologists in more and more exotic terrains. We provide here a few comments, based on our experience, about seismic network deployment and optimization at active landslides. Tripartite seismic arrays are well-suited for apparent velocity and back azimuth determination of an incoming signal (e.g. Joswig, 2008; Vouillamoz, 2015; Sick, 2016), hence providing key information about the source location. Such arrays were used at Super-Sauze and Pechgraben. Because of the rugged and obstructed terrains, as one will encounter at any active landslide, it was not possible to deploy the tripartite arrays with their theoretical optimal geometry (equilateral triangles). Nevertheless, the arrays proved successful in deriving back azimuth and apparent velocity information, using sampling rate of 400 Hz or more. The optimal array aperture was found between 5-10 m. Larger station inter-distances resulted in many small landslide-induced microseismic events not being recorded by all stations, thereby limiting their characterization. Seismic stations housed and installed on a concrete slab for long-term monitoring showed signals similar to those registered by seismic stations simply buried within the ground for short-term monitoring. No significant difference was observed between landslide-induced microseismic signals recorded by stations installed on the active part of the landslide and stations placed on the stable areas surrounding the landslide. Therefore, one may consider installing the seismic network on the stable areas surrounding the landslide for long-term monitoring campaigns to avoid seismic station displacement and tilting.

6.~~1~~ 2 Landslide-induced microseismic events detection and classification

Automatic detection algorithms work fine for well-known routine seismic signatures but fail for unknown and unexpected low-SNR microseismic events. Therefore, in order to gain knowledge about existing landslide-induced microseismic event signatures, we used an enhanced visualization alternative, where continuous seismic data were screened in the form of sonograms for visual pattern recognition (Joswig, 2008; Sick et al., 2012; Vouillamoz et al., 2016). We summarize in Figure 14 the final decision tree applied to the microseismic event classification at clayey landslides, using a minimal number of simple seismic features described in Section 3. (1) A detection was declared for microseismic events observed at a minimum of three seismic stations. (2) A first distinction was made between microseismic events featuring distinct wave packets and events consisting of incoherent sinusoidal signals. The latter gather external sources of tremor-like radiations such as gliding events (airplanes) and environmental noise (rain fronts, storms, wind, creeks…). (3) The decisive discriminating parameter for landslide-induced microseismic events is the slow apparent velocity of distinct wave packets. Events returning fast apparent velocities correspond to external seismic sources, i.e. near, local, regional earthquakes and teleseisms ~~earthquakes~~. (4) Unique events are distinguished from multiple events featuring repeated high-energy jolts, making the separation between micro-quake (type I, II and III) and landslide-induced tremors (ETS-like, rockfall, harmonic and dispersive). (5) The signal duration reflects the source proximity for unique events (the shorter the signal the closer the source). For multiple events, it provides indication about the source size (longer signals carrying more energies). (6) Important waveform amplitude attenuation patterns (S > 200 %) are evidence of a nearby source (receiver-source distance of less than about 50 m) (Section 5.2). This is consistent with the observation that near, local and regional earthquakes don't show S values above 200 %. Incoherent waveform amplitude patterns were typically observed for external sources of tremor radiations (gliding and environmental signals). (7) Characteristics in the frequency content such as dominant frequency above 50 Hz (e.g. band-pass filtered waveforms in Fig. 4a,), harmonics (e.g. unfiltered waveform and amplitude spectrum in Fig. 6c), dispersive dominant energies (e.g. spectrograms in Fig. 7a), gliding frequencies (e.g. spectrogram in Fig. 8b) or multiple frequency bands (e.g. spectrograms in Fig. 8c) enabled the last specification about the end-member event classes. (8) Detected events were gathered in a final catalog of microseismicity at clayey landslides.

Shallow installation of seismic stations in the landslide body results in high level of noise contamination of the data, rendering detection and distinction of landslide-induced microseismic events and other environmental (or anthropological) sources difficult. Seismic signal signatures of proximal sources show important variations among different stations records, as a function of changing receiver-source distance (e.g. Figs. 3a-b, 5a-c and 7). Despite many landslide-induced microseismic events were observed in temporal sequences, hence suggesting a common source process, a cross-correlation analysis performed in the time domain (1-30 Hz band-pass filter) returned no evidence of similar events among the considered sequences. This stresses the complexity and variability of signals radiated by near-source area microseismic processes at clayey landslides. Individual microseismic sources can also occur simultaneously on a complex debris slide, thereby leading to time-overlapping tremor signals with hybrid characteristics where individual source radiations cannot be

unambiguously separated. For example, several quakes doublets (type II and III), similar to short-duration ETS-like signals were observed at both landslides. At Pechgraben, frequent near quakes (type I and II) featuring short duration harmonics were observed. Thus, we conclude that an unequivocal classification of landslide-induced microseismic signals is possible for well-defined, high-quality end-member signals. For complex and hybrid events, input from the analyst is still requisite and larger datasets will be needed, in particular to train automated classifiers.

6.~~2~~ 3 Landslide-induced microseismic event location and interpretation

Due to the high uncertainties - scaling with the landslide dimension itself - of arrival-time based source location of landslide-induced microseismic events (Section 5.1), the receiver-source distance of landslide-induced microseismic events was constrained qualitatively using amplitude information and no maps of landslide-induced microseismicity were produced. Events featuring S values above 200, 1000 and 2000 % were inferred to be recorded in receiver-source distance of less than about 50, 20 and 10 m, respectively, according to calibration tests performed at both landslides (Section 5.2). For these near-source area microseismic events, observations of high-SNR signal spectral content above 50 Hz in the band-pass filtered waveforms or in the amplitude spectrum corroborated a nearby source.

Quake events are inferred to be generated by a single rupture process. Type I and type II quakes feature S values above 200 % and signal duration of less than 2 s. Thus, they are considered to be generated in less than 50 m distance. The slow apparent velocities (< 2.0 km s^{-1}) of the signals are consistent with velocities estimated for clay-rich landslide material (Williams and Pratt, 1996; Tonnellier et al., 2013) and corroborate a source originated within or at the edge of the landslide body. However, one cannot discriminate between both, because location uncertainty is too high and a depth estimation is not possible. S values above 1000 %, higher frequency content, shorter signal duration and few station records of type I events (Fig. 4a and 4e (upper panel)) likely reflect a small and very close source (< 10-20 m). Low-frequency content and longer duration of type II events may account for slower rupture velocity and larger rupture area (Fig. 4b). Type III and type IV events feature S values which are below 200 % and must represent a continuous transition ~~to~~ of quake events recorded at larger receiver-source distances. The higher apparent velocities of wave packets of type IV events and the consistent signal amplitudes of well distinguishable successive phases across the seismic network suggest a source origin outside of the landslide body in the host rock.

The complexity and frequent hybrid characteristics of observed tremor signals make their interpretation challenging. Previous studies interpreted ETS-like signals as being generated by stick-slip (near-repeating quakes) at shear boundaries of the landslide or through fissure development or clogging at the landslide surface (e.g. Gomberg et al., 2011; Walter et al., 2012; Tonnellier et al., 2013). At Super-Sauze and Pechgraben, ETS-like events were mainly observed to occur in temporal sequences; at Pechgraben, alternately with harmonic tremors. Models to explain harmonic tremors include resonance of fluid/gas driven cracks (e.g. (Chouet, 1988; Schlindwein et al., 1995) as well as stick-slip (i.e. swarms of small repeating earthquakes) (e.g. Helmstetter et al., 2015; Lipovsky and Dunham, 2016). Therefore, we postulate stick-slip episodes as the most common source of ETS-like and harmonic tremor signal sequences but cannot exclude fissure formation or clogging as

a mechanism to produce ETS-like signals. Rockfall events produce signals consisting of spikes and jolts, in some instance very similar to ETS-like tremors. Since potential source areas of rockfall can be observed in the field, multiple-spike microseismic signals returning back azimuth towards such areas can be classified as rockfall signals with good certainty. However, in the absence of additional constraints, an unambiguous classification of rockfall and ETS-like signal can be difficult, in particular when the signals are of low-quality. The dispersive character of waveforms and dominant frequencies of dispersive tremors suggest a moving source (Section 4.3.2). Animals as a potential moving source can be excluded with good certainty since signals triggered by animals show spikier patterns, comparable to human footsteps (Fig. 8b and 9a). The inferred source area of dispersive tremors is difficult to access at Super-Sauze and extremely marshy at Pechgraben and no animals or animal traces could be observed there in day time. Debris flows were observed neither in the field nor in daily ground-based and UAV imagery and photo-monitoring in the affected areas. At SZ10, a secondary rotational slide and crown cracks opening were observed near the inferred source area during the detection period of the signals. Such a source mechanism would be compatible with field observations made in the potential source area of dispersive tremors at Pechgraben. Thus, we postulate rotational sliding initiation and/or opening of crown crack(s) as a potential source trigger for the dispersive tremors.

6.~~3~~ 4 Landslide-induced microseismicity rates

Only near-source area quakes type I and II and tremors events (ETS-like, rockfall, harmonic and dispersive) with S > 200% were used in the $M_{L\text{-}LS}$ catalog of landslide-induced microseismicity. This catalog was used to evaluate average daily rates of landslide-induced microseismicity to be compared to average daily displacement rates of the three seismic campaigns (Section 2). The Figure 15 shows the temporal $M_{L\text{-}LS}$ distribution of the near-source area landslide-induced microseismic events for SZ10 (a), PG15 (b) and PG16 (c) and the cumulated number of events curves with $M_{L\text{-}LS}$ > -1 (d). The corresponding average daily landslide-induced microseismicity rates, for $M_{L\text{-}LS}$ > -1 and $M_{L\text{-}LS}$ > 0, show an increase with increasing average daily displacement rates of the three campaigns (e). No relation was found between the energy radiated by local and regional earthquakes (maximum vertical trace absolute amplitude) and the occurrence of landslide-induced microseismic events. At all campaigns, temporal clustering of near-source area landslide-induced microseismic events was observed, especially for tremor signals. Sequences typically last a few minutes to a few hours and are followed by quiescent times. However, higher resolution displacement data (< daily) will be required to better decipher a potential correlation between displacement rates and landslide-induced microseismicity.

7 Conclusion and outlook

We propose a unified typology of microseismic signals observed at slow-moving clay-rich debris slides by comparing passive seismic recordings of three campaigns carried out at two landslides and using published similar case studies as a benchmark. The highly heterogenous and water-saturated state of the material within the slides result in strongly attenuated

and scattered waveforms. Signals generally consists of complex and intricated surface waves, where P- and S-phases cannot be clearly distinguished and successive phase (or wave packets) onsets are difficult, if not impossible to pick. Therefore, simple waveform and spectral attributes of the signals were used for the classification (Section 3 and Fig. 14). The principal discriminating parameters we find to differentiate landslide-induced microseismic signals from unrelated external sources are (1) the low apparent velocity (< 2 km s^{-1}) of trackable wave packets that applies for landslide-induced signals generated in 0-500 m (estimated) receiver-source distances and (2) the prominent and consistent waveform amplitude attenuation patterns of near-source area events across the recording seismic network (Section 5.2). Despite the complexity of the waveforms, comparable landslide-induced microseismic signals were detected at both landslides, suggesting that similar microseismic source processes are taking places at different landslides and that the method is therefore scalable and reproducible. Two main classes of landslide-induced signals were found: (1) quake-like signals and (2) a variety of tremor signals (Sections 4.2-4.3). Because arrival-time based approaches to event location at clayey landslides result in unacceptable level of location uncertainties, waveform amplitude attenuation patterns were used to better constrain receiver-source distances so that $M_{L\text{-}LS}$ could be computed for near-source area events (< about 50 m), applying a distance attenuation function calibrated for clayey landslides (Section 5.3). Results show an increase of daily landslide-induced microseismicity rates with higher average daily displacement rates. Although much attention was paid to derive unbiased magnitude catalogs, uncertainties are still high. In addition, the catalogs may be incomplete in the lower magnitude range due to incomplete datasets (see Section 2). Consequently, we did not derive b-values.

Since passive seismic methods alone do not allow a detailed characterization of microseismic source processes taking place at clayey landslides, seismic data should be supplemented with high spatial-temporal resolution remote sensing, geodetic, geotechnical, geophysical, meteorological and hydrological measurements. A major inconvenient is that ground-based measurements on the landslide during the day result in high anthropological noise level, corrupting a significant part of day-time seismic measurements, when other measurements are available. The seismic monitoring of SZ10, PG15 and PG16 were part of multi-disciplinary field experiments and future directions of this study involve a detailed comparison of microseismic measurements with the other acquired datasets. The aim will be to precisely evaluate the degree to which the main limitation of passive seismic monitoring (high spatial uncertainty of the detected microseismic events and hence speculative sources characterization) can effectively be compensated by remote sensing and other geodetic and geotechnical information. The landslide-induced microseismic event catalog also provides an initial signal library to train future automatic detection systems and classifiers of complex and hybrid microseismic signals at clayey landslides. In addition to Random Forest supervised classifier already implemented by Provost et al. (2017) at Super-Sauze, unsupervised pattern recognition (e.g. Sick et al., 2015) or Hidden Markov Models (e.g. Hammer et al., 2012; Hammer et al., 2013) should be tested and success rates as well as method reproducibility and scalability benchmarked.

Data and resources

The Super-Sauze and Pechgraben passive seismic datasets used in this study are stored at the Institute of Geophysics of the University of Stuttgart, Germany, in SEG-2 and MSEED data format. Request to these data as well as to the catalog of microseismic events can be addressed to the authors. Computations and plots were done with MATLAB® (www.mathworks.com/products/matlab, last accessed November 10, 2017) under a campus license of the University of Stuttgart.

Acknowledgements

This work was funded by an early postdoc mobility fellowship of the SNSF (Swiss National Science Foundation, grant P2FRP2_158749). Birgit Jochum, David Ottowitz and Robert Supper of the Geological Survey of Austria in Vienna are warmly acknowledged for sharing datasets and providing insightful tips and help for the field work in Pechgraben. Jon Mosar of the Institute of Earth Sciences of the University of Fribourg, Switzerland is thanked for lending seismometers and dataloggers for the Pechgraben seismic campaigns. The authors are very grateful to Clément Hibert, Jean-Philippe Malet and Floriane Provost of the EOST, University of Strasbourg, France, for fruitful inputs into this project as well as for sharing datasets and codes. The authors thank Marco Walter, Ulrich Schwaderer and Patrick Blascheck of the Institute for Geophysics (IfG) of the University of Stuttgart for their support at Super-Sauze 2010 seismic monitoring campaign and their help in the microseismic data pre-process. Juan-Carlos Santoyo Campus (IfG, University of Stuttgart) is warmly thanked for his essential participation to the 2015 Pechgraben field campaign. The authors would like to greatly acknowledge the Editor, Fabian Walter (Laboratory of Hydraulics, Hydrology and Glaciology, ETH-Zurich, Switzerland) and the two reviewers, Emma Suriñach (Department of Earth and Ocean Dynamics. Faculty of Earth Sciences. University of Barcelona (UB)~~Department of Geodynamics and Geophysics, University of Barcelona, Spain~~) and Andreas Köhler (Department of Geosciences, University of Oslo, Norway) for their thorough reviews of this manuscript which have help to improve the paper.

Tables and Figures

Table 1. Seismic features of microseismic signal types detected at slow-moving clay-rich debris slides. Features are indicated for high-SNR high-energy signals.

	Signal duration	Signal onset	Attenuation pattern	Dominant frequency	Number of recording station	Max. amplitude [order in nm s^{-1}]	S [%]
Earthquakes							
Local/Regional	~10-60 s	impulsive	none	1-20 Hz	all	10,000	< 200
Tele	minutes	emergent	none	< 5 Hz	all	100	< 100
Quakes							
Type I Near high frequency	<1 s	impulsive	clear	20-100 Hz	< 5	1,000-10,000	200-10,000
Type II Near low frequency	1-2 s	impulsive	clear	5-50 Hz	all	1,000-10,000	200-10,000
Type III Moderate distance	~2 s	impulsive	ambiguous	5-50 Hz	all	1,000	< 200
Type IV Local micro-quake	2-10 s	impulsive	ambiguous	5-50 Hz	all	1,000	< 200
Tremors							
Landslide-induced tremor-like signals							
ETS-like	<20 s	emergent	clear	5-50 Hz	<5-all	1,000-10,000	200-10,000
Confirmed rockfall	5-10 s	emergent	clear	5-100 Hz	<5-all	100-10,000	200-10,000
Harmonic	<5 s	emergent	clear	5-20 Hz	<5	100-1,000	200-1’000
Dispersive	30-120 s	emergent	clear	50-250 Hz	<5-all	10,000	200-100’000
External source of tremor-like radiations							
Footsteps	5 s-minutes	emergent	clear	5-100 Hz	< 5-all	10,000	> 200-10,000
Gliding frequency	20 s-minutes	emergent	none	50-100 Hz	all	1000	100-1,000

Environmental	20 s-minutes	emergent	ambiguous	20-250 Hz	all	10,000	> 200-10,000

Table 2. Three simplified layered v_P velocity models at clayey landslides.

Layer thickness [m]	Model 1	Model 2	Model 3
10	0.4 km s^{-1}	0.65 km s^{-1}	0.8 km s^{-1}
Half-space	2.3 km s^{-1}	1.5 km s^{-1}	2.3 km s^{-1}

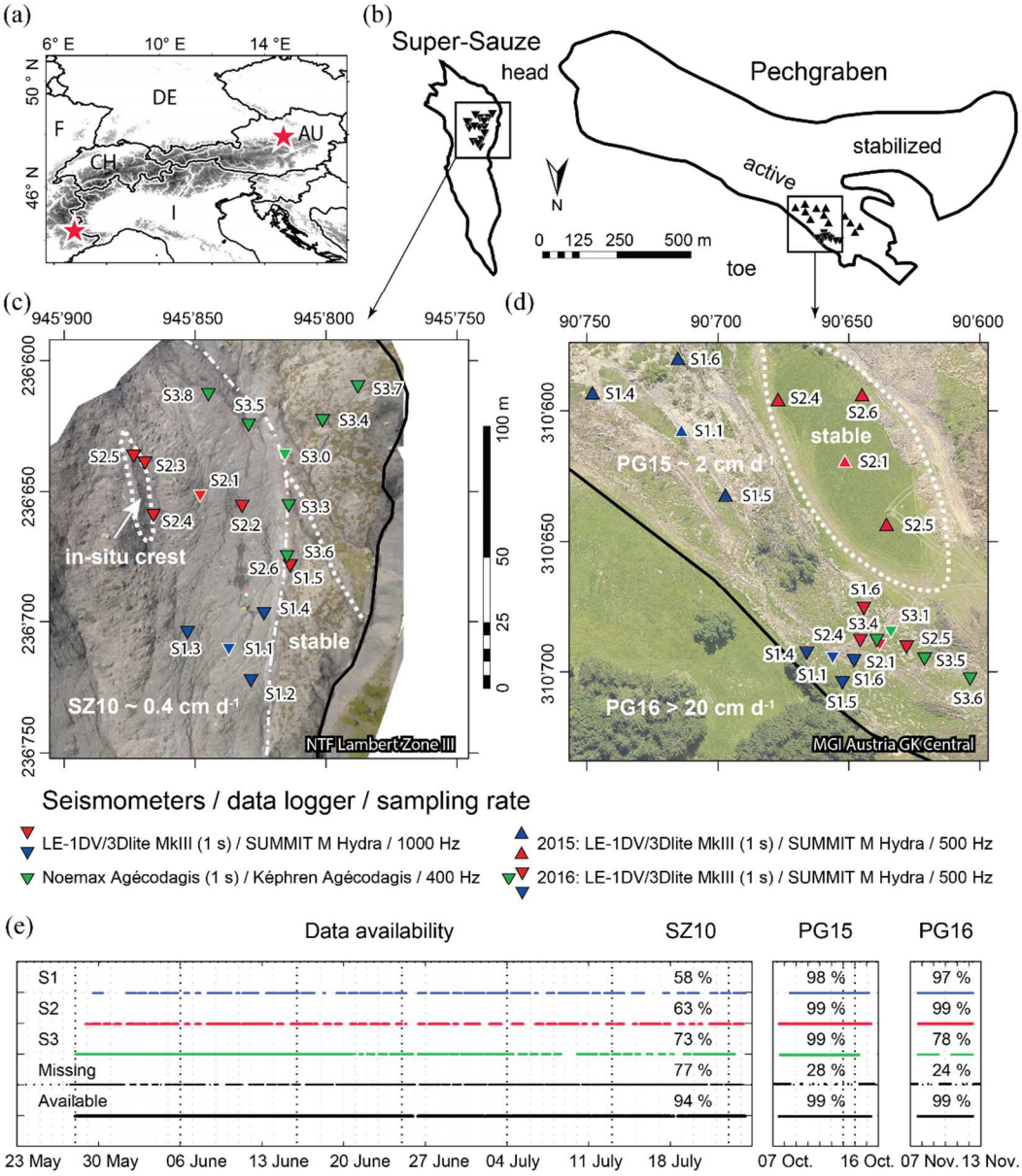

Figure 1. Data overview. (a) Location of Super-Sauze (Southeastern France) and Pechgraben (Upper Austria) clayey landslides (stars). (b) Orthogonal projection of Super-Sauze and Pechgraben instabilities with situation of instrumented areas during the three field campaigns SZ10, PG15 and PG16. (c-d) Zoom into Super-Sauze and Pechgraben seismic networks, where triangles indicate the seismic stations and colors refer to different tripartite arrays (S1, blue; S2, red; and S3, green). The average daily displacement rates prevailing during individual field campaigns are indicated; white dashed lines indicate main subparts of the landslide and black bold lines show the limits of the landslides. 3-C seismometers (S1.1, S2.1, S3.0 and S3.1) are highlighted by white outlines. Orthophotos credits: Super-Sauze, Rothmund et al. (2017); Pechgraben, Lindner et al. (2014); Lindner et al. (2016). (e) Data records availability for individual seismic arrays based on 2 min data segments. The *missing* line indicates incomplete records (measurements from one or two arrays are missing); the *available* line shows where at least one array is recording.

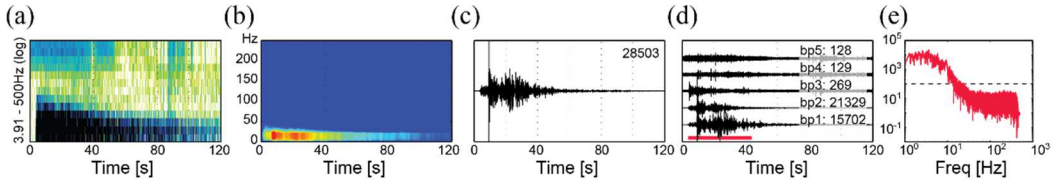

Figure 2. Seismic features of an earthquake in different representations. Regional event (in 110 km distance) of June 30, 2010 11:53 with M_L 4.3 at Saint-Jean-de-Maurienne, France, recorded at SZ10, station S2.1 at t_0 2010.06.30 11:54:00. (a) Sonogram (log Hz). (b) Spectrogram (0-250 Hz). (c) Unfiltered seismogram (nm s^{-1}). (d) Band-pass filtered seismograms (nm s^{-1}, bp1: 1-5; bp2: 5-20; bp3: 20-50; bp4: 50-100; bp5: 100-200 Hz). (e) Amplitude spectrum (FFT, nm Hz^{-1}). A reference line at 100 nm Hz^{-1} help signal comparison. This layout is applied to all figures presenting the microseismic signals classification. Time indication is always UTC. Waveforms maximum absolute 0-to-peak amplitudes are indicated in nm s^{-1} above the seismograms in (c) and (d). The signal window for which the FFT is computed is indicated by the red horizontal line in (d).

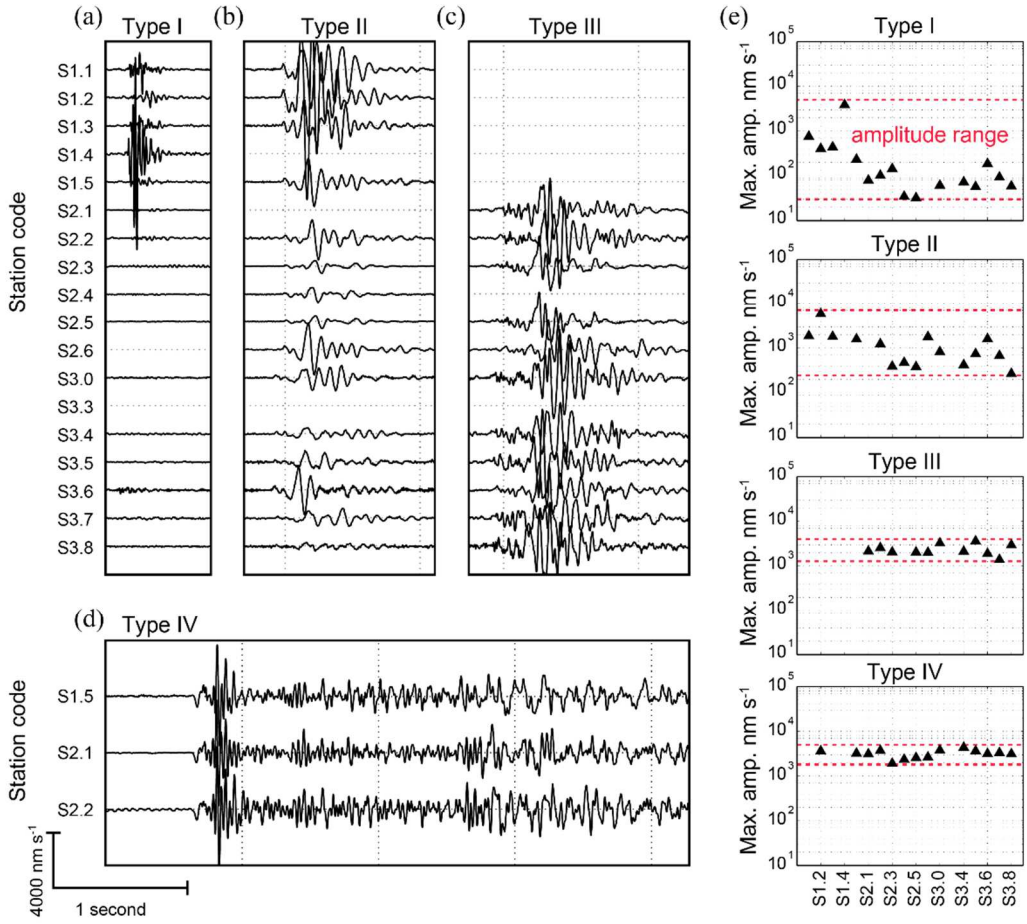

Figure 3. Vertical trace seismograms of quake events recorded at SZ10 (see station location and nomenclature in Figure 1, empty traces correspond to missing or corrupted records). A constant amplitude and time scale are applied to all waveforms (bottom left). (a) Near high frequency quake type I (May 29, 2010, 23:05:05). (b) Near low frequency quake type II (June 26, 2010, 18:44:55). (c) Moderate distance quake type III (June 17, 2010, 15:32:45). (d) Local micro-quake type IV (June 7, 2010 11:24:29). Note the highly coherent successive phases and moderate scattering. (e) Maximum amplitudes (log nm s^{-1}) recorded at individual stations for the four events displayed in a-d. Large amplitude ranges (i.e. important waveform amplitude attenuation, indicated by dashed red lines) enable to discriminate events types I and II from events type III and IV which typically feature narrow amplitude ranges.

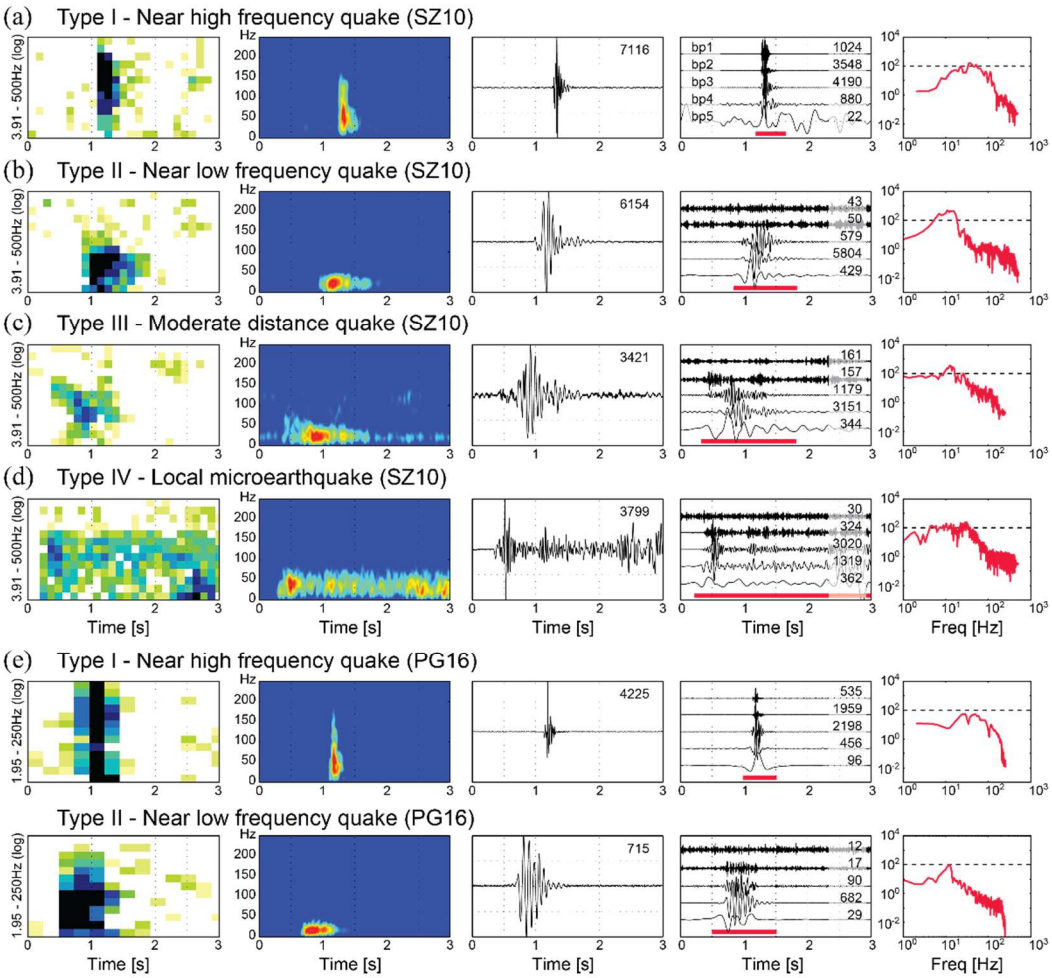

Figure 4. (a-d) Seismic features of the highest SNR/amplitude trace of events presented in Figure 3 and corresponding to type I-type IV quakes. (a) Type I, SZ10, S1.4, t_0 2010.05.29 23:05:04. (b) Type II, SZ10, S1.2, t_0 2010.06.26 18:44:55. (c) Type III, SZ10, S3.0, t_0 2010.06.17 15:32:45.500. (d) Type IV, SZ10, S2.1, t_0 2010.06.07 11:24:29.300. (e) Example of near quakes recorded at Pechgraben. Top: Type I, PG16, S2.6, t_0 2016.11.07 22:43:05.500. Bottom: Type II, PG16, S1.4, t_0 2016.11.09 01:50:13.

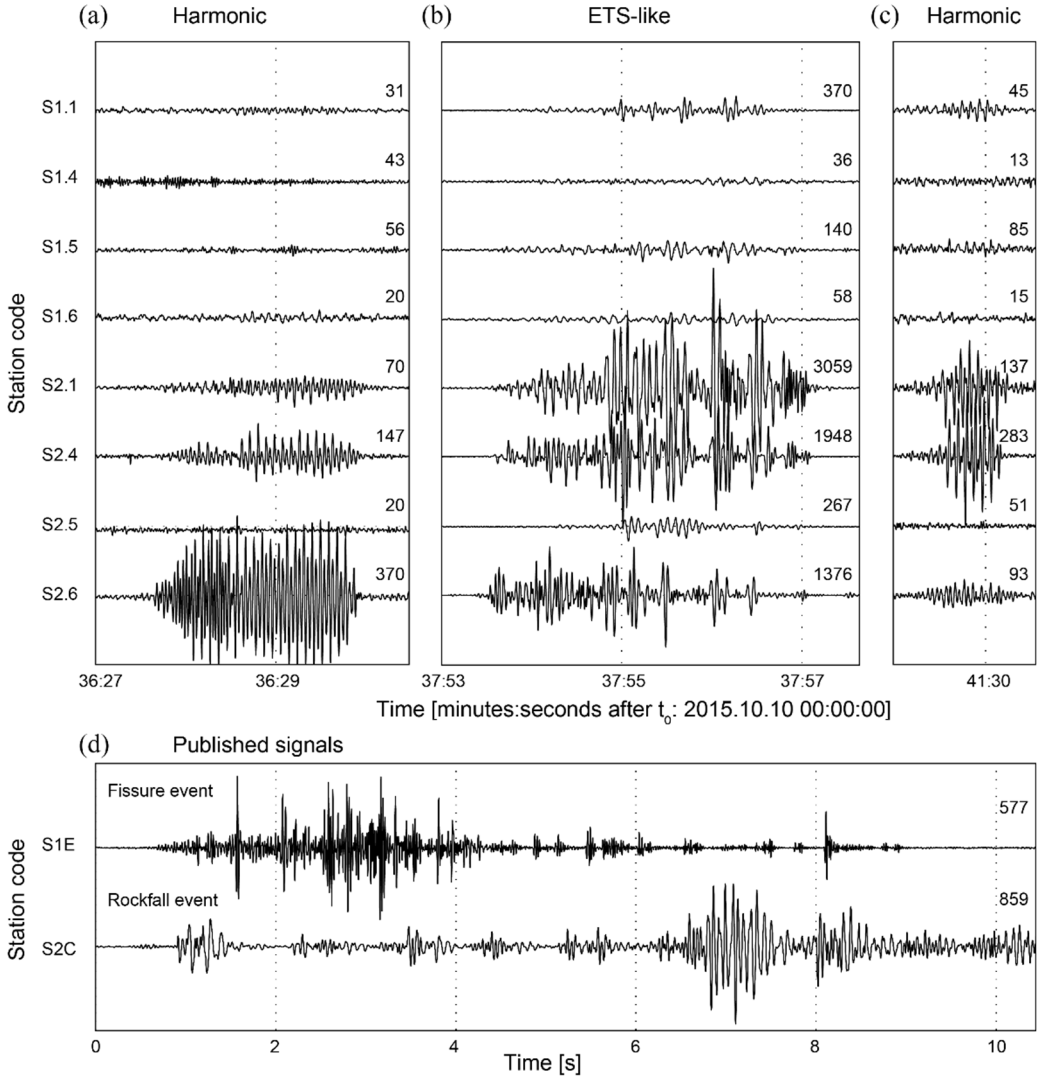

Figure 5. (a-c) Vertical trace seismograms featuring selected signals of a 40 minutes long tremor sequence recorded October 10, 2015 between 00:35 and 01:15 at PG15. See station nomenclature in Figure 1. Waveforms are normalized to the highest amplitude trace of individual events and maximum absolute 0-to-peak amplitudes are given in nm s^{-1} on top of each seismogram. Event (a) and (c) are harmonic tremors, event (b) corresponds to an ETS-like event. Note the prominent attenuation of the waveforms and the relatively lower amplitudes of harmonic tremors. (d) Signals published in Walter et al. (2012) and interpreted as a fissure event (top, t_0 2008.07.14 23:48:40) and a rockfall event (bottom, t_0 2008.07.14 23:49:04). Waveforms are plotted using the same time scale as in a-c to facilitate the signal comparison.

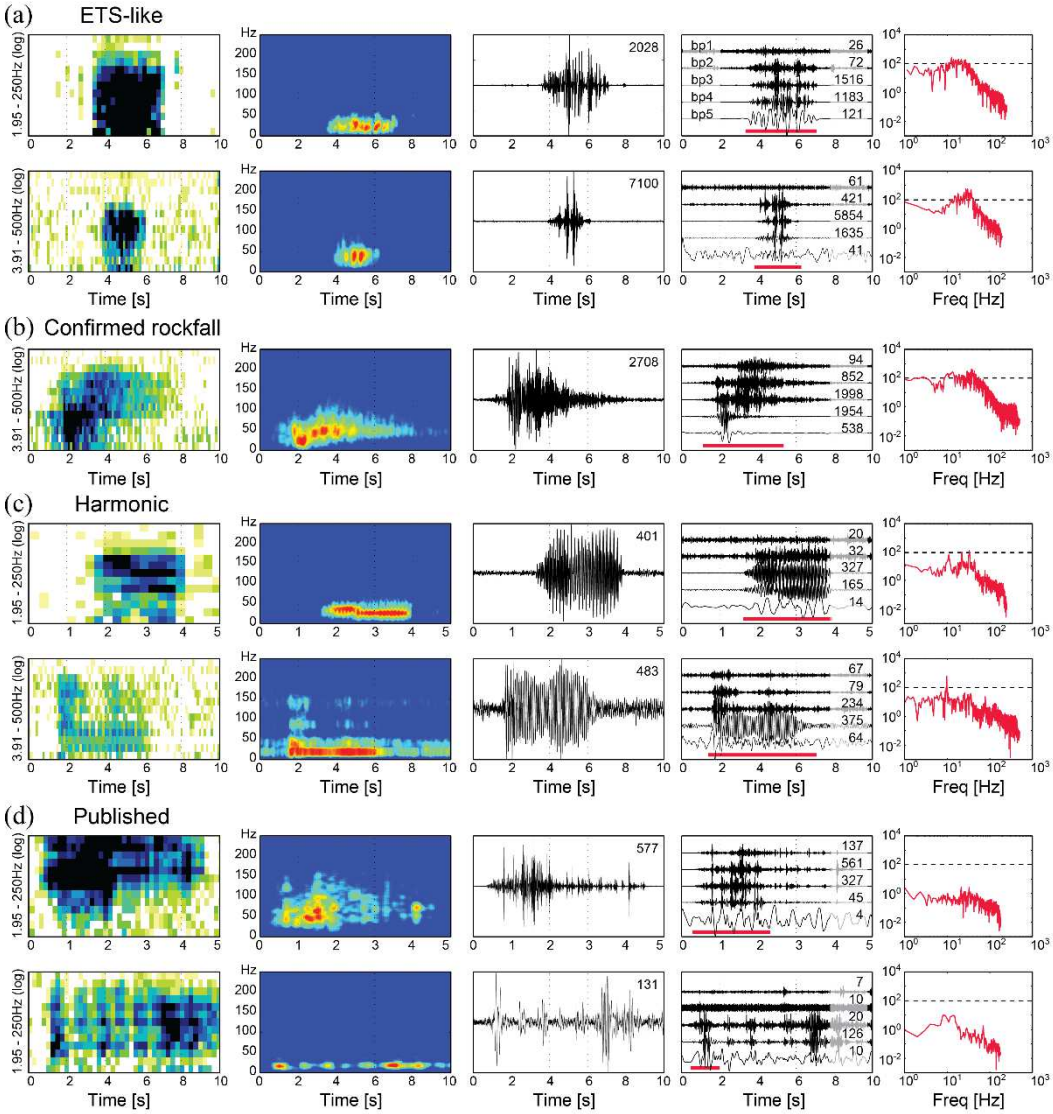

Figure 6. Seismic features of moderate duration (< 20 s) tremor signals recorded at Super-Sauze and Pechgraben. (a) ETS-like events. Top: PG15, S2.4, t_0 2015.10.10 00:37:50. Bottom: SZ10, S3.4, t_0 2010.06.05 15:26:35. (b) Confirmed rockfall event at receiver-source distance of 29 m (Rothmund et al., 2017), SZ10, S2.5, t_0 2010.06.04 06:45:20. (c) Harmonic tremors. Top: PG15, S2.6, t_0 2015.10.10 00:36:26. Bottom: SZ10, S2.3, t_0 2010.06.04 20:07:28. (d) Published tremor signals by Walter et al. (2012). Top: fissure event, t_0 2008.07.14 23:48:40. Bottom: rockfall event, t_0 2008.07.14 23:49:04.

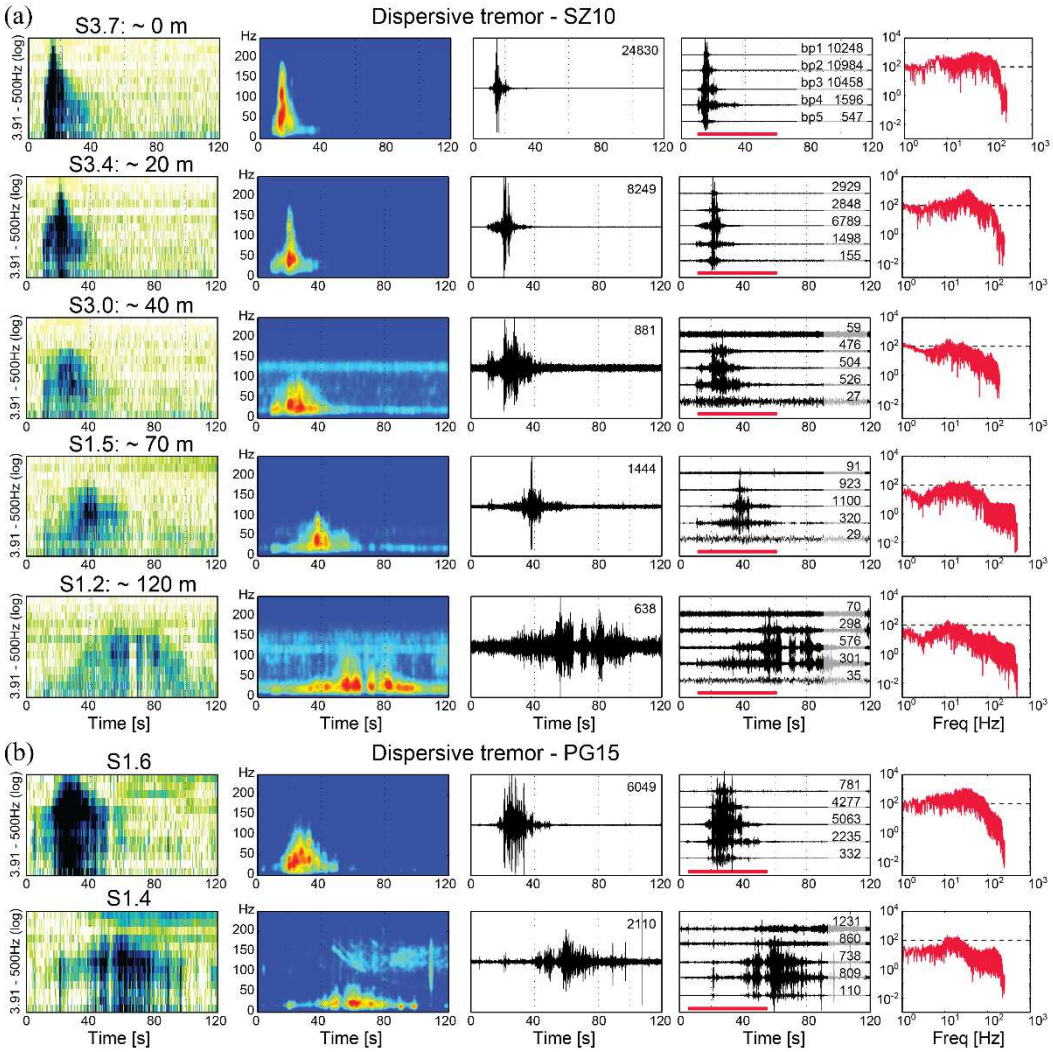

Figure 7. Seismic features of two dispersive tremor events recorded at (a) SZ10 at t_0 2010.07.04 00:45:20 and (b) PG15 at t_0 2015.10.08 18:02:08. Stations are indicated on top of the sonogram panels and displayed in (a) and (b) from top to bottom with increasing inferred distance to the most probable source area (SZ10 stations S3.7 and S1.2 are about 120 m distant; PG15 stations S1.6 and S1.4 are about 50 m distant, the receiver-source distance could not be estimated). Note the noise contamination by an airplane (gliding harmonics in the spectrogram) well visible at PG15 station S1.4. The airplane signal was well recorded by the complete seismic network, whereas the dispersive event is only seen at array S1 stations.

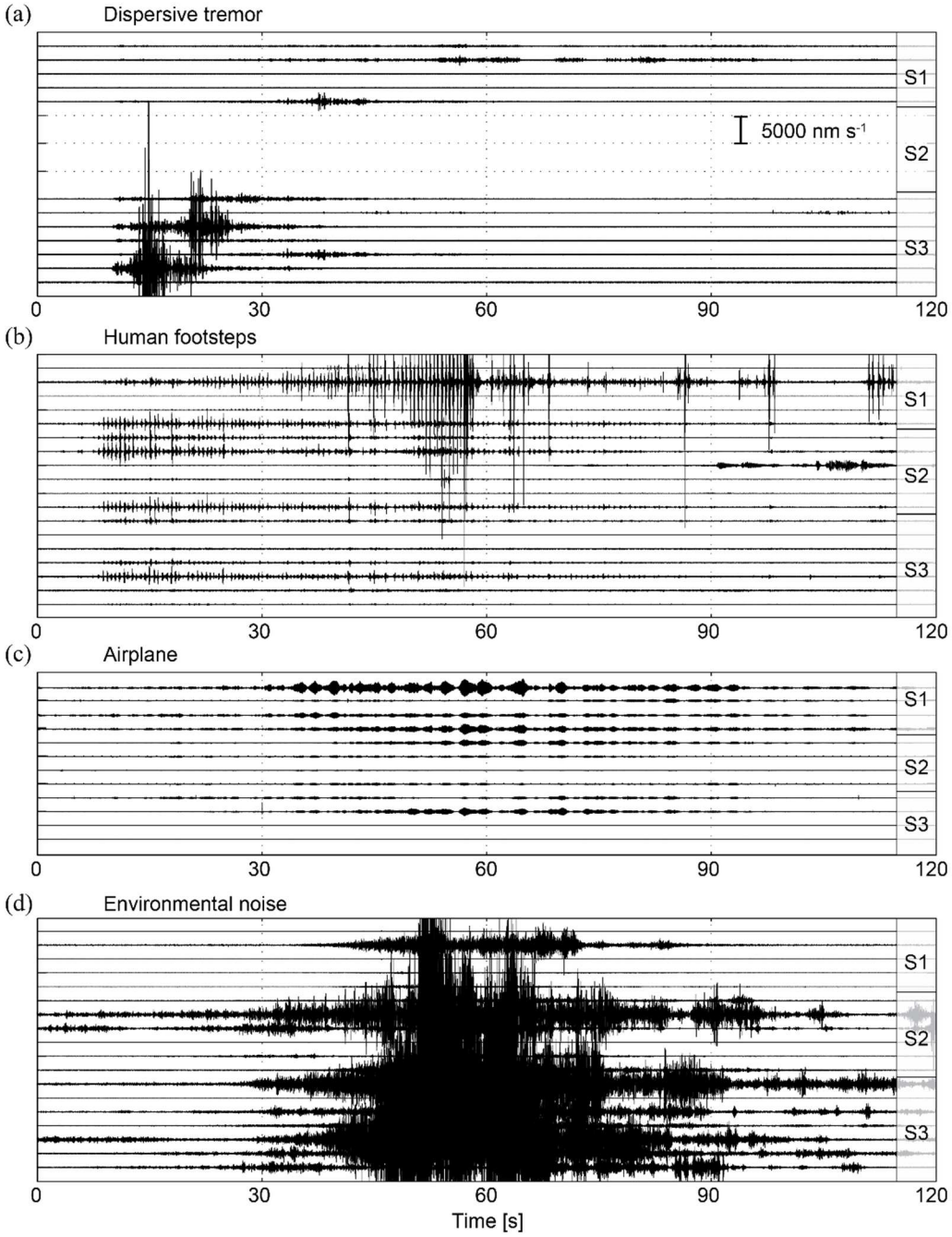

Figure 8. Vertical trace seismograms of long duration tremor-like signals recorded at Super-Sauze and Pechgraben. A constant time and amplitude scale (indicated in (a)) are applied. (a) Dispersive tremor, SZ10, t0 2010.07.04 00:45:20. (b) Human footsteps at short distances, SZ10, t_0 2010.06.05 13:08:33. (c) Airplane, PG16, t_0 2016.11.08 04:56:00. (d) Environmental noise, SZ10, t_0 2010.06.09 22:54:10.

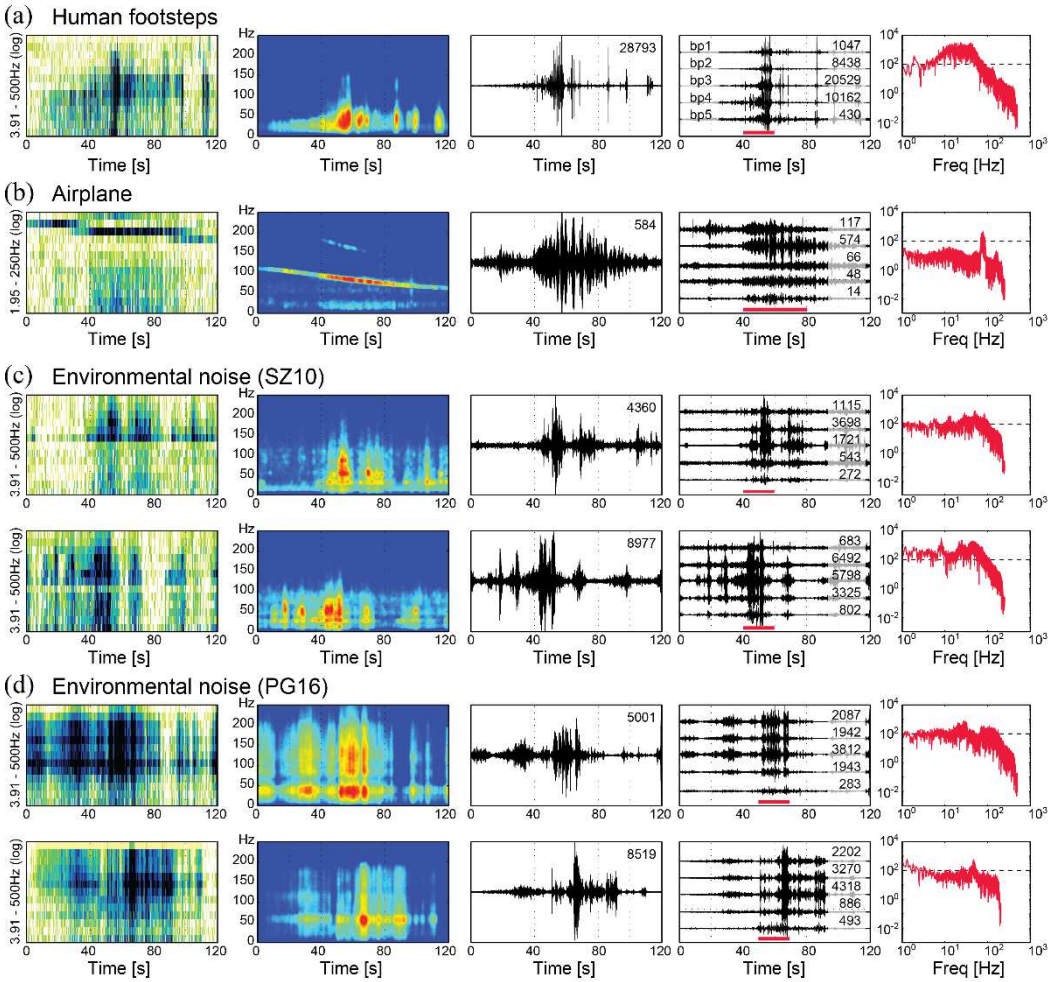

Figure 9. Seismic features of the most common external sources of tremor-like radiations. (a) Human footsteps at short distance at SZ10, S1.2, t_0 2010.06.05 13:08:33. (b) Airplane at PG16, S2.1, t_0 2016.11.08 04:56:00 with typical gliding harmonics in the spectrogram. (c) Environmental noise recorded at SZ10, stations S2.3 (top) and S3.8 (bottom) at t_0 2010.06.09 22:54:10 and (d) at PG16, stations S2.1 (top) and S3.1 (bottom) at t_0 2016.11.08 03:00:40.

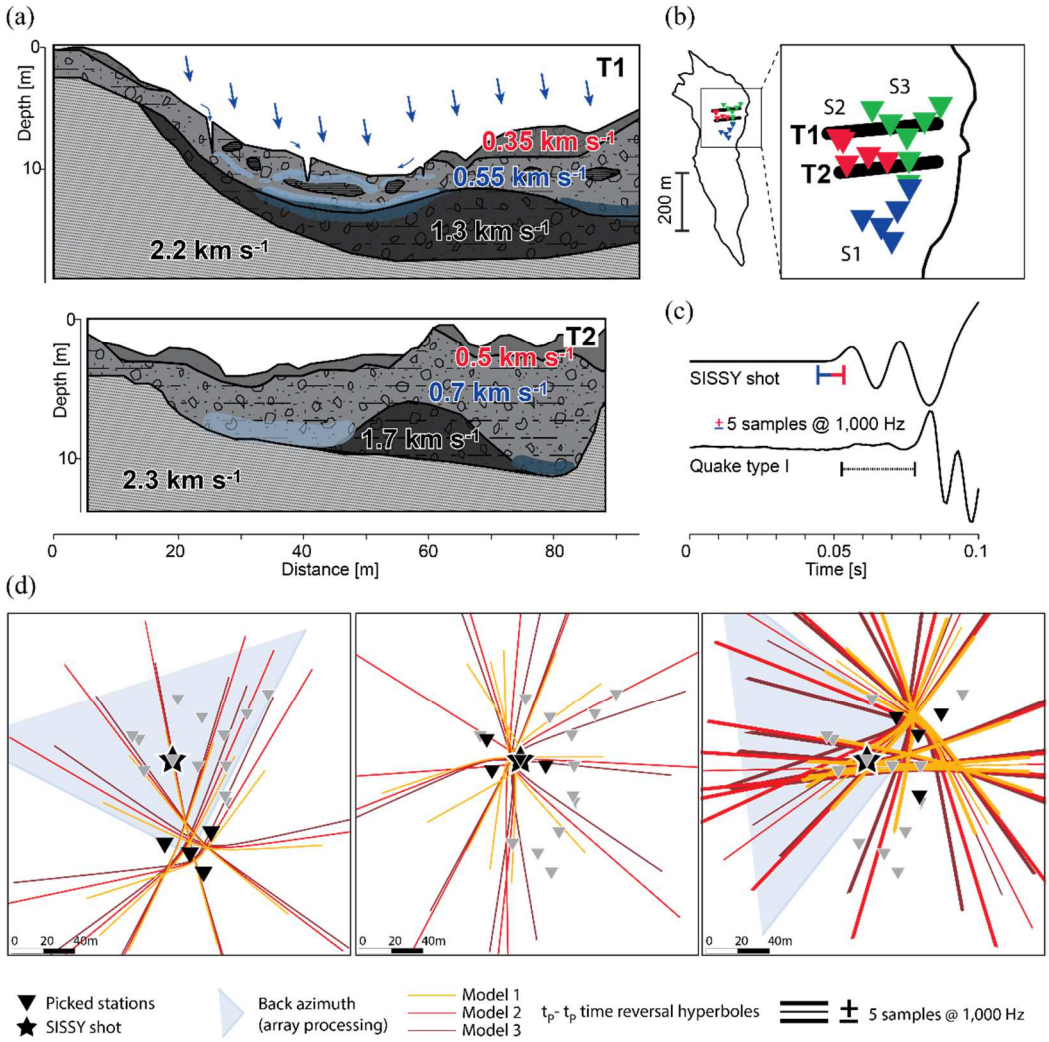

Figure 10. Parameters impacting arrival-time based location uncertainties at clayey landslides. (a) Complex seismic velocity structures along two tomographic profiles T1 and T2 at Super-Sauze; modified from Tonnellier et al. (2013) and Gance et al. (2016). (b) Location of the tomographic profiles T1 and T2 within the seismic arrays S1, S2, S3. (c) High-quality first arrival of a SISSY calibration shot (top trace, SZ10, S2.2, t_0 2010.06.04 11:56:22) and first arrival of a high-SNR quake type I event (bottom trace, SZ10, 2010.05.29 23:05:03). Note the higher uncertainties about the onset of the natural event. (d) Graphical location solutions for the SZ10 SISSY calibration shot at station S2.1, June 4, 2010, 11:56:22 derived from first arrivals at individual seismic array S1 (left panel), S2 (middle panel) and S3 inner ring (right panel). Picked stations are indicated by black triangles, beam-processing results are symbolized by shaded light-blue quadrants, time-reversal hyperboles derived with three different velocity models (Table 2) are represented by orange, red and brown lines. In the right panel, bold hyperboles image the effect of ± five samples uncertainties offset shifts in first arrivals. Discussion is found in Section 5.1.

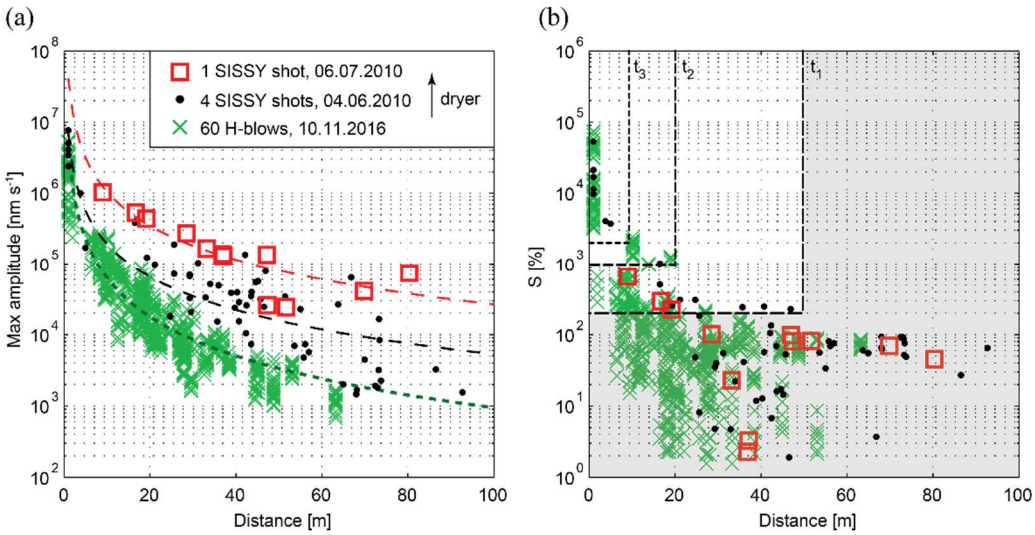

Figure 11. (a) Maximum absolute 0-to-peak amplitudes with distance to the source of SISSY calibration shots carried out at Super-Sauze June 4 (dots) and July 6 (squares), 2010, and hammer blows (crosses) carried out at Pechgraben, November 10, 2016. Dashed lines indicate log-log regression curves. Note the lower attenuation with dryer conditions. (b) Scatter about the median amplitude (S) of the calibration datasets presented in (a). S values of natural events higher than 200, 1000 and 2000 % are inferred to image receiver-source distances of about 50, 20 and 10 m (t_1 t_2 t_3) respectively.

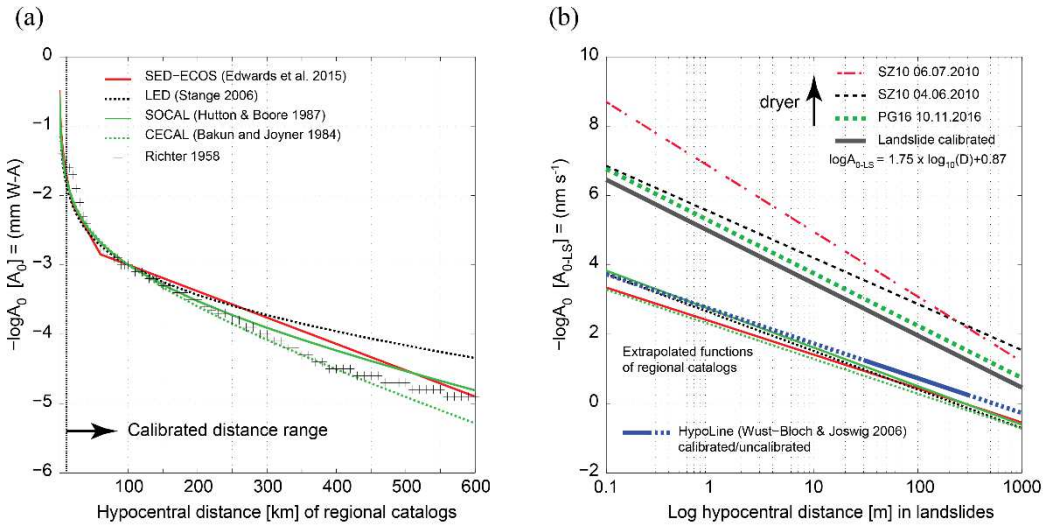

Figure 12. (a) Distance attenuation functions (-log(A_0)) of M_L scales empirically calibrated for regional earthquakes with receiver-source distances between 10 and 600-1000 km. (b) Log-log zoom into the valid receiver-source distance range of microseismic observations at clayey landslides. The HypoLine distance attenuation function, which was calibrated between 30-300 m in the Dead Sea Valley (Wust-Bloch and Joswig, 2006) is very similar to the projection of the regional M_L scales. The distance attenuation regression curves derived from SISSY calibration shots and hammer blows data (see Figure 11) project in the upper area of the graphic, all with steeper slopes (imaging stronger attenuation) than the regional M_L scales. The landslide calibrated distance attenuation function applies an average slope of 1.75 with an intercept of 0.87. Note that regional M_L scales use displacement amplitudes in WA mm, whereas $M_{L\text{-}LS}$ scale is calibrated using velocity readings in nm s^{-1}, hence a direct comparison of these curves is not straightforward. Discussion is found in Section 5.3.

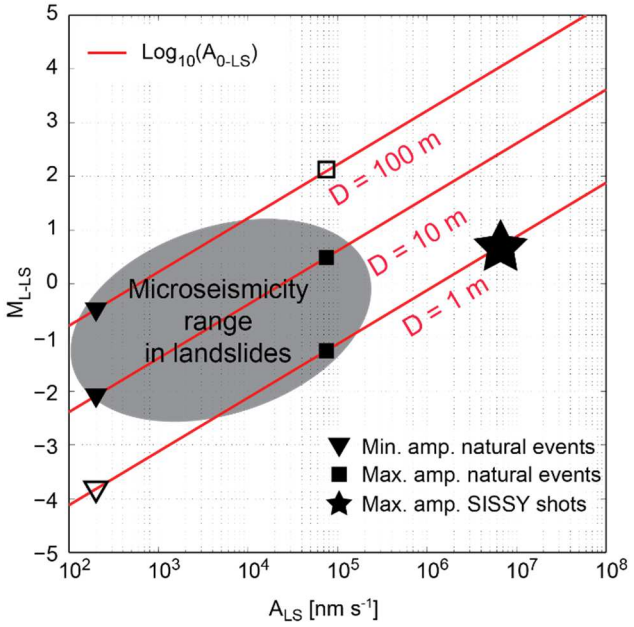

Figure 13. $M_{L\text{-}LS}$ as a function of amplitude reads in 1, 10 and 100 m receiver-source distances. The star indicates the average maximum amplitude reads of SISSY calibration shots in 1 m distance that corresponds to $M_{L\text{-}LS}$ 0.58. Minimum and maximum signal amplitudes observed for landslide-induced signals are symbolized by triangles and squares respectively. Empty symbols indicate lower probability valid distances of low and high amplitude values. A reasonable field of potential $M_{L\text{-}LS}$ of landslide-induced microseismic events is outlined by the shaded ellipse.

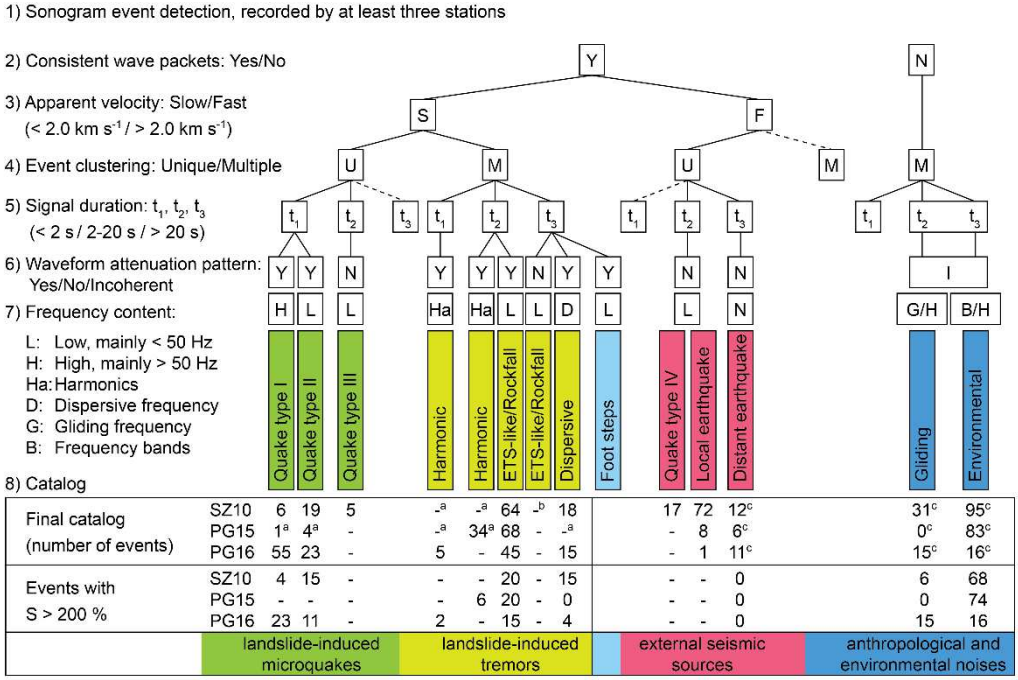

		Quake type I	Quake type II	Quake type III	Harmonic	Harmonic	ETS-like/Rockfall	ETS-like/Rockfall	Dispersive	Foot steps	Quake type IV	Local earthquake	Distant earthquake	Gliding	Environmental
Final catalog (number of events)	SZ10	6	19	5	-[a]	-[a]	64	-[b]	18		17	72	12[c]	31[c]	95[c]
	PG15	1[a]	4[a]	-	-[a]	34[a]	68	-	-[a]		-	8	6[c]	0[c]	83[c]
	PG16	55	23	-	5	-	45	-	15		-	1	11[c]	15[c]	16[c]
Events with S > 200 %	SZ10	4	15	-	-	-	20	-	15		-	-	0	6	68
	PG15	-	-	-	-	6	20	-	0		-	-	0	0	74
	PG16	23	11	-	2	-	15	-	4		-	-	0	15	16
		landslide-induced microquakes			landslide-induced tremors						external seismic sources			anthropological and environmental noises	

Figure 14. (1-7) Final decision-tree for microseismic events classification at clayey landslides. (8) Catalog with number of detection for each class (top frame) and number of near-source area events with S > 200 % (bottom frame). Indices indicate (a) fields in which such events were detected, but recorded at less than three seismic stations; (b) fields were such events were observed at other fields campaigns (e.g. Walter et al., 2012); and (c) fields unrelated to the landslide microseismicity, where only the higher SNR events were catalogued. Discussion is found in Section 6.3.

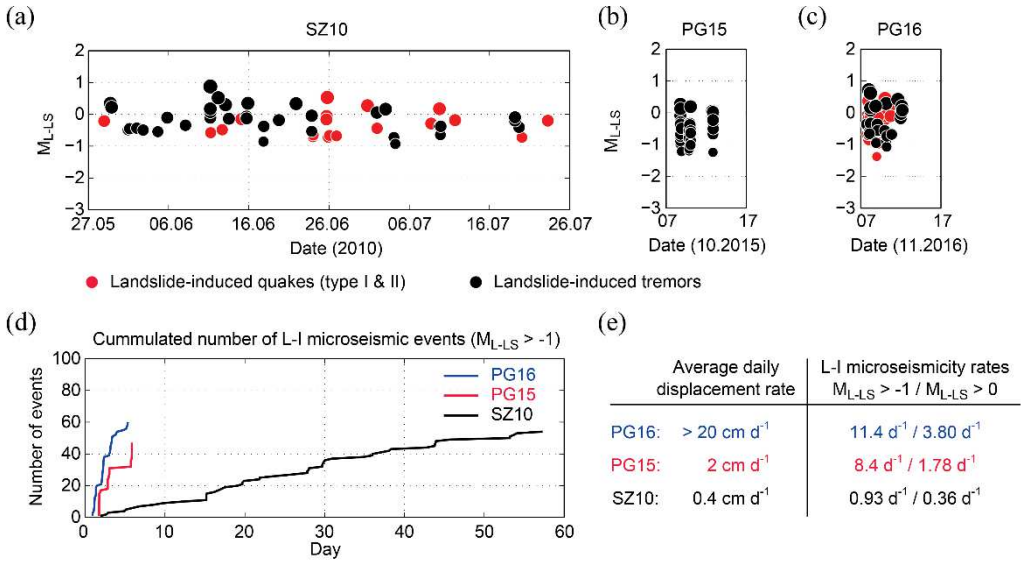

Figure 15. (a-c) Temporal distribution of M_{L-LS} for near-source area (< 50 m) landslide-induced microseismic events at SZ10 (a), PG15 (b) and PG16 (c). Red circles show quake events type I and II and black circles indicate landslide-induced tremors (ETS-like, rockfall, harmonic and dispersive with S > 200 %). The time scale is constant in all plots. (d) Cumulative number of landslide-induced microseismic events with S > 200 % curves for M_{L-LS} > -1 events. (c) Daily landslide-induced microseismicity rates for M_{L-LS} > -1 and M_{L-LS} > -0 show an increase with higher average daily displacement rates.

References

Aki, K. and Richards, P. G.: Quantitative seismology, 2nd ed., University Science Books, Sausalito, Calif., Great Britain, 2002.

Bakun, W. H. and Joyner, W. B.: The ML scale in Central California, Bulletin of the Seismological Society of America, 74, 1827–1843, 1984.

Battaglia, J.: Location of seismic events and eruptive fissures on the Piton de la Fournaise volcano using seismic amplitudes, J. Geophys. Res., 108, 615, doi:10.1029/2002JB002193, 2003.

Battaglia, J., Aki, K., and Ferrazzini, V.: Location of tremor sources and estimation of lava output using tremor source amplitude on the Piton de la Fournaise volcano: 1. Location of tremor sources, Journal of Volcanology and Geothermal Research, 147, 268–290, doi:10.1016/j.jvolgeores.2005.04.005, 2005.

Beard, F. D.: Predicting slides in cut slopes, Western Construction, San Fransisco, 36, 72, 1961.

Biescas, B., Dufour, F., Furdada, G., Khazaradze, G., and Suriñach, E.: Frequency Content Evolution of Snow Avalanche Seismic Signals, Surv Geophys, 24, 447–464, doi:10.1023/B:GEOP.0000006076.38174.31, 2003.

Brückl, E., Brunner, F. K., Lang, E., Mertl, S., Müller, M., and Stary, U.: The Gradenbach Observatory—monitoring deep-seated gravitational slope deformation by geodetic, hydrological, and seismological methods, Landslides, 10, 815–829, doi:10.1007/s10346-013-0417-1, 2013.

Brückl, E. and Mertl, S.: Seismic monitoring of deep-seated mass movements, Disaster Mitigation of Debris Flows, Slope Failures and Landslides, Universal Academy Press, Inc. Tokyo, Japan, 571–580, 2006.

Cadman, J. D. and Goodman, R. E.: Landslide noise, Science, 158, 1182–1184, doi:10.1126/science.158.3805.1182, 1967.

Chouet, B.: Resonance of a Fluid-Driven Crack: Radiation Properties and Implications for the Source of Long-Period Events and Harmonic Tremor, Journal of Geophysical Research, 93, 4375–4400, 1988.

Deichmann, N.: Theoretical Basis for the Observed Break in ML / Mw Scaling between Small and Large Earthquakes, Bulletin of the Seismological Society of America, 107, 505–520, doi:10.1785/0120160318, 2017.

Diehl, T., Kissling, E., Husen, S., and Aldersons, F.: Consistent phase picking for regional tomography models: application to the greater Alpine region, Geophysical Journal International, 176, 542–554, doi:10.1111/j.1365-246X.2008.03985.x, 2009.

Eberhardt, E., Spillmann, T., Maurer, H., Willenberg, H., Loew, S., and Stead, D.: The Randa Rockslide Laboratory: Establishing brittle and ductile instability mechanisms using numerical modelling and microseismicity, 9th International Symposium of Landslides, Rio de Janeiro, A. A. Balkema, Leiden, 481–487, 2004.

Edwards, B., Kraft, T., Cauzzi, C., Kastli, P., and Wiemer, S.: Seismic monitoring and analysis of deep geothermal projects in St Gallen and Basel, Switzerland, Geophysical Journal International, 201, 1022–1039, doi:10.1093/gji/ggv059, 2015.

Eibl, E. P.S., Lokmer, I., Bean, C. J., and Akerlie, E.: Helicopter location and tracking using seismometer recordings, Geophysical Journal International, 209, 901–908, doi:10.1093/gji/ggx048, 2017.

Eibl, E. P.S., Lokmer, I., Bean, C. J., Akerlie, E., and Vogfjörd, K. S.: Helicopter vs. volcanic tremor: Characteristic features of seismic harmonic tremor on volcanoes, Journal of Volcanology and Geothermal Research, 304, 108–117, doi:10.1016/j.jvolgeores.2015.08.002, 2015.

Fischer, T., Roth, M., and Kühn, D.: Seismic monitoring of a rock slope Åknes, Norway: time-reversal localization of seismic activity, Geophysical Research Abstracts, 16, 2014.

Gance, J., Malet, J.-P., Supper, R., Sailhac, P., Ottowitz, D., and Jochum, B.: Permanent electrical resistivity measurements for monitoring water circulation in clayey landslides, Journal of Applied Geophysics, 126, 98–115, doi:10.1016/j.jappgeo.2016.01.011, 2016.

Gomberg, J., Bodin, P., Savage, W., and Jackson, M. E.: Landslide faults and tectonic faults, analog?: The Slumgullion earthflow, Colorado, Geology, 23, 41–44, 1995.

Gomberg, J., Schulz, W., Bodin, P., and Kean, J.: Seismic and geodetic signatures of fault slip at the Slumgullion Landslide Natural Laboratory, Journal of Geophysical Research, 116, doi:10.1029/2011JB008304, 2011.

Hammer, C., Beyreuther, M., and Ohrnberger, M.: A Seismic-Event Spotting System for Volcano Fast-Response Systems, Bulletin of the Seismological Society of America, 102, 948–960, doi:10.1785/0120110167, 2012.

Hammer, C., Ohrnberger, M., and Fah, D.: Classifying seismic waveforms from scratch: a case study in the alpine environment, Geophysical Journal International, 192, 425–439, doi:10.1093/gji/ggs036, 2013.

Helmstetter, A. and Garambois, S.: Seismic monitoring of Séchilienne rockslide (French Alps): Analysis of seismic signals and their correlation with rainfalls, J. Geophys. Res., 115, doi:10.1029/2009JF001532, 2010.

Helmstetter, A., Moreau, L., Nicolas, B., Comon, P., and Gay, M.: Intermediate-depth icequakes and harmonic tremor in an Alpine glacier (Glacier d'Argentière, France): Evidence for hydraulic fracturing?, J. Geophys. Res. Earth Surf., 120, 402–416, doi:10.1002/2014JF003289, 2015.

Hotovec, A. J., Prejean, S. G., Vidale, J. E., and Gomberg, J.: Strongly gliding harmonic tremor during the 2009 eruption of Redoubt Volcano, Journal of Volcanology and Geothermal Research, 259, 89–99, doi:10.1016/j.jvolgeores.2012.01.001, 2013.

Hungr, O., Leroueil, S., and Picarelli, L.: The Varnes classification of landslide types, an update, Landslides, 11, 167–194, doi:10.1007/s10346-013-0436-y, 2014.

Hutton, L. K. and Boore, D. M.: The ML scale in southern California, Bulletin of the Seismological Society of America, 77, 2074–2094, 1987.

Jolly, A. D., Thompson, G., and Norton, G. E.: Locating pyroclastic flows on Soufriere Hills Volcano, Montserrat, West Indies, using amplitude signals from high dynamic range instruments, Journal of Volcanology and Geothermal Research, 118, 299–317, 2002.

Jones, G. A., Kulessa, B., Doyle, S. H., Dow, C. F., and Hubbard, A.: An automated approach to the location of icequakes using seismic waveform amplitudes, Ann. Glaciol., 54, 1–9, doi:10.3189/2013AoG64A074, 2013.

Joswig, M.: Pattern recognition for earthquake detection, Bulletin of the Seismological Society of America, 80, 170–186, 1990.

Joswig, M.: Automated classification of local earthquake data in the BUG small array, Geophysical Journal International, 120, 262–286, 1995.

Joswig, M.: Pattern recognition techniques in seismic signal processing, in Proc. 2. workshop AI in seismology and engineering seismology, Cahiers Centre Europ. Geodyn. Seism., 12, 37–56, 1996.

Joswig, M.: Nanoseismic monitoring fills the gap between microseismic networks and passive seismic, special topic, Leveraging Technology, first break, 26, 117–124, 2008.

Jurich, D. M. and Miller Russell J.: Acoustic monitoring of landslides, Geotechnology, Transportation Research Record, 30–38, 1987.

Koerner, R. M., McCabe, W. M., and Lord, A. E.: Acoustic Emission Behavior and Monitoring of Soils, in: Acoustic Emissions in Geotechnical Engineering Practice, Drnevich, V. P., and Gray, R. E. (Eds.), ASTM International, 100 Barr Harbor Drive, PO Box C700, West Conshohocken, PA 19428-2959, 93-93-49, 1981.

Kumagai, H., Palacios, P., Maeda, T., Castillo, D. B., and Nakano, M.: Seismic tracking of lahars using tremor signals, Journal of Volcanology and Geothermal Research, 183, 112–121, doi:10.1016/j.jvolgeores.2009.03.010, 2009.

Lacroix, P. and Helmstetter, A.: Location of Seismic Signals Associated with Microearthquakes and Rockfalls on the Sechilienne Landslide, French Alps, Bulletin of the Seismological Society of America, 101, 341–353, doi:10.1785/0120100110, 2011.

Lindner, G., Schraml, K., Mansberger, R., and Hübl, J.: UAV monitoring and documentation of a large landslide, Appl Geomat, 8, 1–11, doi:10.1007/s12518-015-0165-0, 2016.

Lindner, G., Schraml, K., Ottowitz, D., Jochum, B., Gruber, H., and Tartarotti, T.: Monitoring im Bereich des Erdschuttstroms Pechgraben (Oberösterreich): Methodik und Ergebnisse, Journal for Torrent, Avalanche, Landslide and Rock Fall, 73, 2014.

Lipovsky, B. P. and Dunham, E. M.: Tremor during ice-stream stick slip, The Cryosphere, 10, 385–399, doi:10.5194/tc-10-385-2016, 2016.

Malet, J.-P., Laigle, D., Remaître, A., and Maquaire, O.: Triggering conditions and mobility of debris flows associated to complex earthflows, Geomorphology, 66, 215–235, doi:10.1016/j.geomorph.2004.09.014, 2005.

Mertl, S. and Brückl, E.: Observation of fracture processes in creeping rock masses by seismic monitoring, in: Proceedings of 11th Congress of the ISRM, Lisbon, Portugal, 9-13 July 2007, 2007.

National French Landslide Observatory Facility and RESIF Datacenter: French Multidisciplinary Observatory of Versant Instabilities, Université de Grenoble Alpes, 2006.

Provost, F., Hibert, C., and Malet, J.-P.: Automatic classification of endogenous landslide seismicity using the Random Forest supervised classifier, Geophys. Res. Lett., 44, 113–120, doi:10.1002/2016GL070709, 2017.

Richter, C. F.: Elementary Seismology, W.H. Freeman and Co., San Fransisco, 1958.

Röösli, C., Walter, F., Husen, S., Andrews, L. C., Lüthi, M. P., Catania, G. A., and Kissling, E.: Sustained seismic tremors and icequakes detected in the ablation zone of the Greenland ice sheet, J. Glaciol., 60, 563–575, doi:10.3189/2014JoG13J210, 2014.

Roth, M., Dietrich, M., Blikra, L. H., and Lecomte, I.: Seismic monitoring of the unstable rock slope site at Aknes, Norway, NORSAR Report, Oslo, 2005.

Rothmund, S., Vouillamoz, N., and Joswig, M.: Mapping slow-moving alpine landslides by UAV — Opportunities and limitations, The Leading Edge, 36, 571–579, doi:10.1190/tle36070571.1, 2017.

Schlindwein, V., Wassermann, J., and Scherbaum, F.: Spectral analysis of harmonic tremor at Mt. Semeru volcano, Indonesia, Geophysical Research Letters, 22, 1685–1688, 1995.

Sick, B.: Temporal and spectral pattern recognition for detection and combined network and array waveform coherence analysis for location of seismic events, Thesis, Institute for Geophysics, University of Stuttgart, Stuttgart, Germany, 225 pp., 2016.

Sick, B., Guggenmos, M., and Joswig, M.: Chances and limits of single-station seismic event clustering by unsupervised pattern recognition, Geophysical Journal International, 201, 1801–1813, doi:10.1093/gji/ggv126, 2015.

Sick, B., Walter, M., and Joswig, M.: Visual Event Screening of Continuous Seismic Data by Supersonograms, Pure and Applied Geophysics, doi:10.1007/s00024-012-0618-x, 2012.

Spillmann, T., Maurer, H., Green, A. G., Heincke, B., Willenberg, H., and Husen, S.: Microseismic investigation of an unstable mountain slope in the Swiss Alps, Journal of Geophysical Research, 112, doi:10.1029/2006JB004723, 2007.

Stange, S.: ML Determination for Local and Regional Events Using a Sparse Network in Southwestern Germany, Journal of Seismology, 10, 247–257, doi:10.1007/s10950-006-9010-6, 2006.

Tonnellier, A., Helmstetter, A., Malet, J.-P., Schmittbuhl, J., Corsini, A., and Joswig, M.: Seismic monitoring of soft-rock landslides: the Super-Sauze and Valoria case studies, Geophysical Journal International, 193, 1515–1536, doi:10.1093/gji/ggt039, 2013.

Unglert, K. and Jellinek, A. M.: Volcanic tremor and frequency gliding during dike intrusions at Kīlauea-A tale of three eruptions, J. Geophys. Res. Solid Earth, 120, 1142–1158, doi:10.1002/2014JB011596, 2015.

van Herwijnen, A. and Schweizer, J.: Monitoring avalanche activity using a seismic sensor, Cold Regions Science and Technology, 69, 165–176, doi:10.1016/j.coldregions.2011.06.008, 2011.

Vouillamoz, N.: Microseismic characterization of Fribourg area (Switzerland) by Nanoseismic Monitoring, Thesis, Department of Geosciences - Unit of Earth Sciences, University of Fribourg, Fribourg, Switzerland, 270 pp., 2015.

Vouillamoz, N., Wust-Bloch, G. H., Abednego, M., and Mosar, J.: Optimizing Event Detection and Location in Low-Seismicity Zones: Case Study from Western Switzerland, Bulletin of the Seismological Society of America, 106, 2023–2036, doi:10.1785/0120160029, 2016.

Walter, F., Burtin, A., McArdell, B. W., Hovius, N., Weder, B., and Turowski, J. M.: Testing seismic amplitude source location for fast debris-flow detection at Illgraben, Switzerland, Nat. Hazards Earth Syst. Sci., 17, 939–955, doi:10.5194/nhess-17-939-2017, 2017.

Walter, M., Arnhardt, C., and Joswig, M.: Seismic monitoring of rockfalls, slide quakes, and fissure development at the Super-Sauze mudslide, French Alps, Engineering Geology, 128, 12–22, doi:10.1016/j.enggeo.2011.11.002, 2012.

Walter, M. and Joswig, M.: Seismic monitoring of fracture processes generated by a creeping landslide in the Vorarlberg Alps, first break, 26, 131–135, 2008.

Walter, M. and Joswig, M.: Seismic characterization of slope dynamics caused by softrock-landslides: the Super-Sauze case-study, in: Proceedings of the International Conference on Landslide Processes: from geomorphologic mapping to dynamic modelling, Malet, J.-P., Remaître, A., and Boogard, T. A. (Eds.), CERG Editions, Strasbourg, 215–220, 2009.

Walter, M., Walser, M., and Joswig, M.: Mapping Rainfall-Triggered Slidequeakes and Seismic Landslide-Volume Estimation at Heumoes slope, Vadose Zone Journal, 10, 487–495, 2011.

Williams, R. A. and Pratt, T. L.: Detection of the base Slumgullion landslide, Colorado, by seismic reflection and refraction methods, in: The Slumgullion Earth Flow: A Large-Scale Natural Laboratory, Varnes, D. J., and Savage, W. Z. (Eds.), U.S. Geol. Surv. Bull., 2130, 77–84, 1996.

Wust-Bloch, G. H. and Joswig, M.: Pre-collapse identification of sinkholes in unconsolidated media at Dead Sea area by ‘nanoseismic monitoring’ (graphical jackknife location of weak sources by few, low-SNR records), Geophysical Journal International, 167, 1220–1232, doi:10.1111/j.1365-246X.2006.03083.x, 2006.

Yamasato, H.: Quantitative Analysis of Pyroclastic Flows Using Infrasonic and Seismic Data at Unzen Volcano, Japan, Journal of Physics of the Earth, 45, 397–416, 1997.